

# 1 Quantify and reduce flood forecast uncertainty by the CHUP- 2 BMA method

3 Zhen Cui<sup>1</sup>, Shenglian Guo<sup>1\*</sup>, Hua Chen<sup>1</sup>, Dedi Liu<sup>1</sup>, Yanlai Zhou<sup>1</sup>, Chong-Yu Xu<sup>2</sup>

4 <sup>1</sup> State Key Laboratory of Water Resources Engineering and Management, Wuhan University, Wuhan, China

5 <sup>2</sup> Department of Geoscience, University of Oslo, Oslo, Norway

6 *Correspondence to:* Shenglian Guo (slguo@whu.edu.cn)

7 **Abstract.** The Bayesian model averaging (BMA), hydrological uncertainty processor (HUP), and HUP-BMA methods have  
8 been widely used to quantify flood forecast uncertainty. This study proposed the CHUP-BMA method by introducing a  
9 copula-based HUP in the framework of BMA to bypass the need for normal quantile transformation of the HUP-BMA  
10 method. The proposed ensemble forecast scheme consists of 8 members (two forecast precipitation inputs, two advanced  
11 long short-term memory (LSTM) models, and two objective functions used to calibrate parameters) and is applied to the  
12 interval basin between Xiangjiaba and Three Gorges Reservoir (TGR) dam-site. The ensemble forecast performance of the  
13 HUP-BMA and CHUP-BMA methods is explored in the 6-168h forecast horizons. The TGR inflow forecasting results show  
14 that the two methods can improve the forecast accuracy over the selected member with the best forecast accuracy, and the  
15 CHUP-BMA performs much better than the HUP-BMA. [Compared with the HUP-BMA method, the forecast interval width  
16 and continuous ranked probability score metrics of the CHUP-BMA method are reduced by a maximum of 28.42% and  
17 17.86% within all forecast horizons, respectively.](#) The probability forecast of the CHUP-BMA method has better reliability  
18 and sharpness and is more suitable for flood ensemble forecasts, providing reliable risk information for flood control  
19 decision-making.

## 20 1 Introduction

21 Accurate and reliable flood forecasting is one of the necessary measures to reduce flood disasters and improve water  
22 resource utilization (Zhou et al., 2019; Vegad and Mishra, 2022). With the development of hydrological theory and flood  
23 forecasting techniques, the flood forecasting accuracy and lead time have been significantly improved in recent years (Xu et  
24 al., 2022; Cui et al., 2023). However, neither physically-based and conceptual hydrological models nor data-driven models  
25 can guarantee to obtain perfect forecasting in real conditions. Because of the influence of the changing environment and the  
26 limitations of human perception of complex hydrological processes, the meteorological forcing and other inputs,  
27 hydrological model structure, and parameters, etc., contain significant uncertainties (Cloke et al., 2009), which leads to the  
28 simulation and forecast results of the model inevitably containing integrated uncertainties from multiple sources (Liu et al.,  
29 2022). Traditional flood forecasting schemes are mostly deterministic forecast results without considering forecast

30 uncertainty (Zhong et al., 2018a; Gelfan et al., 2018), which makes decision-makers unable to grasp useful risk information  
31 beyond the forecast value. Excessive superstition on a single forecast value will likely lead to poor decision-making  
32 (Krzysztofowicz et al., 1999). Therefore, it is essential to quantify and reduce flood forecast uncertainty in practical  
33 applications.

34 Probabilistic flood forecasting is one of the effective methods to quantify integrated forecast uncertainty (Matthews et  
35 al., 2022). It not only provides a deterministic forecast value, but also provides forecast uncertainty (or risk) information by  
36 means of quantile, confidence interval, or density function (Biondi and Todini, 2018; Ferretti et al., 2020; Zhou et al., 2022),  
37 which is more scientifically reasonable and practically useful compared with deterministic forecasts and helps decision-  
38 makers consider forecast risk quantitatively (Todini, 2008). Various probabilistic forecasting methods based on statistical  
39 post-processing of numerical forecast data have been developed in recent years. Among these methods, probabilistic  
40 ensemble forecasting is considered to overcome the limitations of a single model or a simple average with fixed model  
41 weights (Han and Coulibaly, 2017) and contains richer forecast information because it can consider the ensemble forecast  
42 results of multiple models to quantify and reduce integrated uncertainty that contains uncertainties in the inputs, model  
43 structure, and parameters (Li et al., 2017; Saleh et al., 2016). Bayesian model averaging (BMA), proposed by Raftery et al.  
44 (2005), uses the Bayesian theory and a total probability formulation to transform ensemble forecasts into probabilistic  
45 forecasts and is one of the most representative and reliable methods that has been widely used to supplement uncertainty  
46 information beyond point estimates (Shu et al., 2022).

47 [The BMA method has been applied to temperature, precipitation, and wind speed ensemble forecasts of meteorological](#)  
48 [forcing](#) (Raftery et al 2005; Sloughter et al, 2007; Sloughter et al, 2010). After confirming that the BMA method can  
49 effectively quantify forecast uncertainty and obtain highly accurate deterministic forecasts, it is widely used in hydrological  
50 forecasting to quantify forecast uncertainty from different sources, such as model inputs, structure, and parameters. The  
51 standard BMA method assumes that each member's posterior probability distribution approximately obeys a normal  
52 distribution (Huang et al., 2019; Guo et al., 2021). However, some variables, such as wind speed, rainfall, runoff, etc.,  
53 usually obey skewed distributions and require methods such as Box-Cox to convert non-Gaussian variables to standard  
54 normal variables that affect the accuracy of probability distribution estimation (Duan et al., 2007; Liu et al., 2018). Many  
55 authors have investigated the applicability of BMA in flood ensemble forecasting and tried to overcome its limitations  
56 (Madadgar and Moradkhani, 2014; Darbandsari and Coulibaly,2020). Sloughter et al. (2010) proposed an improved BMA  
57 method by assuming that the posterior probability distribution of each member could obey a specific non-normal distribution  
58 (e.g., Gamma distribution) and using the member forecast values to estimate the mean and variance of the distribution.  
59 Madadgar and Moradkhani (2014) introduced the Copula function to solve the posterior probability distribution of members  
60 in the BMA method and proposed the Copula-based BMA method, which avoids the assumption of the posterior probability  
61 distribution and further reduces the application limitation of the BMA method. In order to ensure that the quantiles of  
62 forecast distributions after Box-Cox transformation are within the actual physical range, Baran et al. (2019) introduced upper  
63 and lower truncated normal distributions into the BMA, and found that the double truncated BMA had reliable forecasting

64 ability compared to ensemble model output statistics. The advantage was more obvious when rolling window training  
65 periods are used. Hemri et al. (2013) introduced the principle of geostatistical output perturbation into the BMA method and  
66 proposed a multivariate BMA, which extended the membership probability distribution into a multivariate normal  
67 distribution function. Relative to the univariate BMA method, the multivariate BMA can not only consider the temporal  
68 correlation between forecast flows, but also improve the forecast reliability when the forecast system was changing, i.e.,  
69 fewer models were available due to dropping out at particular lead times. Meanwhile, the BMA method usually ensembles  
70 the forecast results of multiple models to be as close to the actual values as possible. However, too many ensemble members  
71 may generate redundant information. Darbandsari and Coulibaly (2020) introduced the Shannon entropy theory to select the  
72 forecast members that satisfy the above conditions before applying BMA. Their results showed that the BMA method  
73 incorporating entropy could improve the probabilistic forecasting performance for high flows over the standard BMA  
74 method. In addition, some studies have developed various methods based on the BMA principle, such as the multi-model  
75 ensemble forecasting method based on Vine Copula (Zhang et al., 2022) and the combination of BMA and data assimilation  
76 techniques (Parrish et al., 2012).

77 However, most studies ignore an essential issue: the BMA does not consider the constraint of initial conditions (i.e.,  
78 observed flow at the start of the forecast). It can be shown from Raftery et al. (2005) that the conditional distribution of the  
79 member ( $Q_{fi}$ ) in the BMA is assumed to follow the normal distribution with expectation  $\mu_i = a_i + b_i \cdot Q_{fi}$  ( $a_i$  and  $b_i$  are the bias  
80 correction coefficients) and variance  $\sigma_i$ , which implies that the conditional distribution is only related to the member's  
81 forecasted flow and not affected by the observed flow at the forecast start time. It is unreasonable to produce the same  
82 posterior distribution when the forecast results are the same at different moments.

83 The hydrological uncertainty processor (HUP) can obtain the posterior distribution function of the actual value under  
84 the condition of the forecast value and the observed flow at the start time based on Bayesian principles and the assumption of  
85 perfect rainfall forecasting (Krzysztofowicz and Kelly, 2000). Darbandsari and Coulibaly (2021) firstly utilized the HUP  
86 method to derive the posterior distribution of each member considering the initial constraints, and then used the BMA  
87 method to weight the conditional distribution of all members to obtain the final posterior distribution, which is called the  
88 HUP-BMA method. Their results showed that the HUP-BMA method outperforms the HUP method and improves the BMA  
89 method in short-term probabilistic forecasting. In addition, the derivability of the posterior distribution for the ensemble  
90 members is theoretically enhanced, the heteroskedasticity of the ensemble members is considered, and the interpretability  
91 and logical rationality of the BMA method are improved.

92 Although it has been demonstrated that considering initial conditions in the BMA method can improve ensemble  
93 forecast performance, there are still issues to be explored. The HUP-BMA method requires a normal quantile conversion  
94 method to convert the flow data series to Gaussian space to solve the posterior distribution. The process is not only tedious  
95 and complicated, but also prone to bias in the inverse conversion. To this end, Liu et al. (2018) adopted the copula to derive  
96 the conditional distribution of the observed flow under the conditions of the forecasted flow, which avoids the assumption  
97 that the flow series obeys a normal distribution in the HUP and relaxes the application limitation. The study shows that the

98 CHUP can improve the probabilistic forecasting performance of the HUP method. It is anticipated that coupling CHUP to  
99 the BMA may improve the HUP-BMA accuracy and applicability, which motivates the current study.

100 The main innovations and research steps are shown as follows: (1) A novel CHUP-BMA method is proposed for the  
101 first time by coupling CHUP into BMA, which not only avoids the normal distribution assumption in HUP-BMA, but also  
102 considers the constraints of the initial condition of the forecast. (2) An ensemble forecast containing eight members is  
103 constructed by combining two types of forecast precipitation, two long short-term memory (LSTM) models, i.e., the  
104 recursive encoder-decoder structure-based LSTM-RED model and the feature-temporal dual attention-based DA-LSTM-  
105 RED model, and two objective functions of model calibration. (3) The ensemble forecast performance of the proposed  
106 method is analysed and discussed in comparison to the HUP-BMA benchmark method in terms of the deterministic and  
107 probabilistic forecasts. The interval basin between Xiangjiaba Dam and the Three Gorges Dam in the Yangtze River, China,  
108 is selected as case study.

109 The rest of the paper is organized as follows. Section 2 introduces the case study and materials. The methods are  
110 presented in Section 3. Section 4 evaluates the deterministic and ensemble forecast results. Conclusions and prospects are  
111 given in Section 5.

## 112 **2 Case study and materials**

### 113 **2.1 Study basin**

114 Three Gorges Reservoir (TGR) is the largest hydraulic project in the world and plays a vital role in flood control, power  
115 generation, and other water resource management issues (Zhong et al., 2020). The TGR controls a watershed area of about 1  
116 million km<sup>2</sup>. The total reservoir capacity is about 39.3 billion m<sup>3</sup>, with a flood control capacity of about 22.15 billion m<sup>3</sup>.

117 The TGR inflow is directly influenced by the runoff yield of the cascade reservoir interval-basin between Xiangjiaba  
118 and TGR (Fig.1), with a basin area of about 127,400 km<sup>2</sup> (Zhou et al., 2019). The inflow of the TGR consists of the outflow  
119 discharge from the Xiangjiaba Reservoir, the inflow of several tributaries such as Min, Tuo, Jialing, and Wu Rivers, and the  
120 rainfall of the interval-basin. The flow sources are complex and have different effects on the TGR inflow. Moreover, TGR is  
121 a river-type reservoir with a length of about 600 km at the normal storage level (175m) and an average width of only 1.1 km,  
122 resulting in uncertainty in rainfall intensity and storm-centre positioning (Zhong et al., 2020). Therefore, there is significant  
123 uncertainty in the flood forecast of TGR. It has been a major challenge to quantify and reduce forecast uncertainty.

124 Table 1 shows the flow propagation time from the hydrological control stations of the mainstream and tributaries to the  
125 TGR dam. The outflow discharge of Xiangjiaba Reservoir, located on the Jinsha River, is observed at the Pingshan  
126 hydrological station and represents the mainstream flow. The discharge values from large tributaries (Min, Jialing, Tuo, and  
127 Wu Rivers) are observed at the Gaochang, Fushun, Beibei, and Wulong hydrological stations, respectively.

128

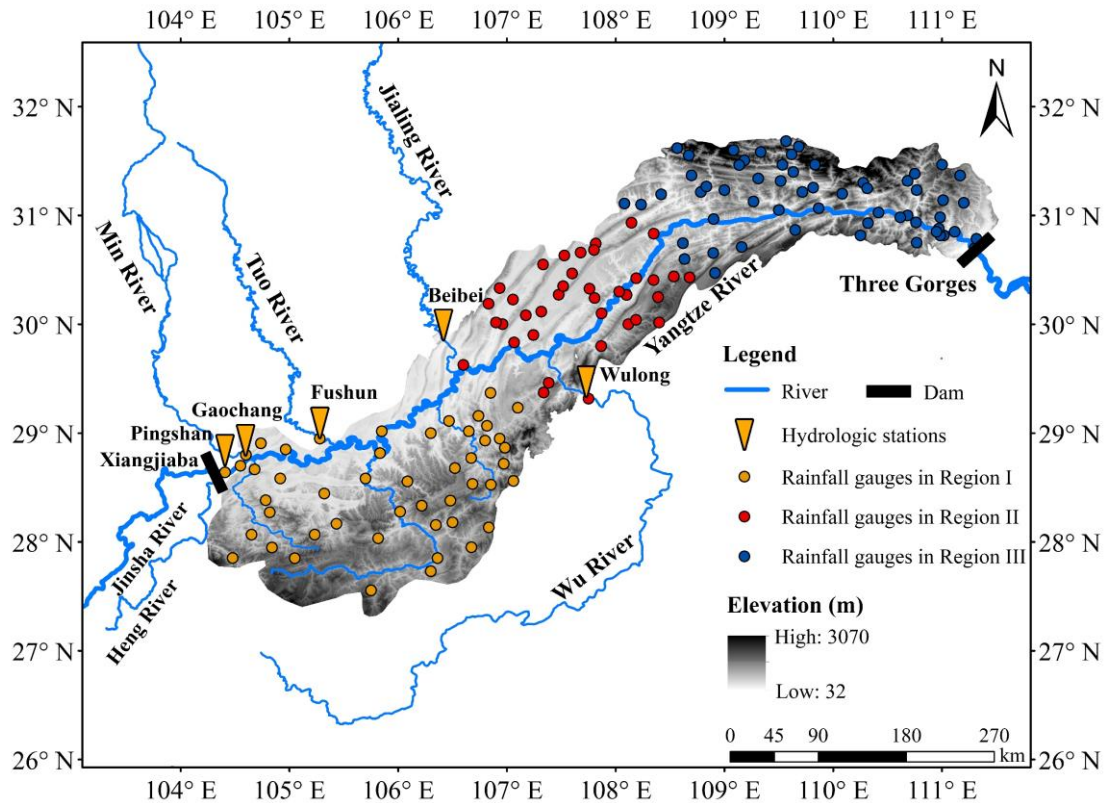


**Fig. 1** Schematic diagram of the interval-basin between Xiangjiaba and TGR dam-site which is divided into three sub-regions.

Considering the uneven distribution of rainfall intensity because of the narrow and long basin, the interval basin between Xiangjiaba and TGR dam-site is divided into three sub-basins: Pingshan-Cuntan, Cuntan-Wanxian, and Wanxian-TGR dam-site. Their watershed areas are 76,900, 22,900, and 27,600 km<sup>2</sup> respectively. Meanwhile, there are 45, 38, and 60 gauged rainfall stations in these three sub-regions, respectively.

**Table 1** List of flow propagation time for hydrological control stations to TGR dam-site

Rivers	Hydrological control stations	To TGR dam flow propagation time (h)
Jinsha	Pingshan	48-66
Min	Gaochang	48-66
Jialing	Beibei	24-42
Tuo	Fushun	42-60
Wu	Wulong	15-30

## 139 2.2 Study materials

140 This study collects 6h observed flow discharges at TGR dam-site and five hydrological stations (Table 1), and 6h  
141 observed rainfall in the interval-basin during the 2010-2021 flood season (May-September). The Tyson polygon method is  
142 used to calculate areal average rainfall using rainfall station data for each sub-basin area. Meanwhile, this study collects the  
143 forecasted precipitation data issued by the European Centre for Medium-Range Weather Forecasts (ECMWF) and the  
144 Hydrology Bureau of the Yangtze River Water Resources Commission (HBWRWC) for the 2017-2021 flood season in the  
145 three sub-basins. Their forecast time starts at 8:00, with the 6-168h forecast horizons and the 6h forecast interval. The spatial  
146 resolution of each grid for the ECMWF forecasted precipitation is  $0.125^\circ \times 0.125^\circ$ . The HBWRWC forecasted precipitation  
147 is the areal average forecasted precipitation data.

148 The training period is from 2010 to 2016, and the validation period is from 2017 to 2021. Since the precipitation  
149 forecast starts at 8:00 a.m., the forecasted flow for the 6-168h forecast horizons is also calculated from the daily 8:00 a.m. in  
150 the validation period.

## 151 3 Methods

### 152 3.1 Proposed CHUP-BMA method

#### 153 3.1.1 Bayesian model averaging (BMA)

154 Bayesian model averaging (BMA) method's principle is as follows.

$$p(Q_o | Q_{f,1}, Q_{f,2}, \dots, Q_{f,k}) = \sum_{i=1}^k w_i \cdot p(Q_o | Q_{f,i}) \quad (1)$$

155 where, where,  $p(\cdot)$  denotes the probability density function.  $Q_o$  denotes the observed flow corresponding to the forecast  
156 moment (target value).  $k$  is the number of ensemble members.  $Q_f$  denotes the forecasted flow of ensemble members.  $w_i$   
157 denotes the weight of the  $i$ -th model.  $p(Q_o | Q_{f,i})$  denotes the conditional probability density of  $Q_o$  conditional on  $Q_{f,i}$ , which is  
158 assumed to approximately obey a normal distribution with the expectation of  $\mu_i = a_i + b_i \cdot Q_{f,i}$  and variance of  $\sigma_i$ .  $a_i$  and  $b_i$  are the  
159 bias correction coefficients obtained by linear fitting of  $Q_{f,i}$  to  $Q_o$ .

160 Therefore, Eq. (1) can be rewritten as follows.

$$p(Q_o | Q_{f,1}, Q_{f,2}, \dots, Q_{f,k}) = \sum_{i=1}^k w_i \cdot N(Q_o | \mu_i, \sigma_i) \quad (2)$$

161 From Eq. (2), it can be seen that the BMA method does not consider the influence of the initial state (the actual  
162 observed flow at the start of the forecast) on the posterior distribution. When the member forecasts at different times are the  
163 same, the posterior probability distribution generated by the BMA is also the same, which lacks logical rationality.

### 164 3.1.2 Hydrological uncertainty processor (HUP)

165 Based on the assumption that the precipitation uncertainty is zero, under the condition that the  $i$ -th ensemble member  
 166 forecasts ( $Q_{f,i}$ ) and the observed flow at the start of the forecast ( $Q_b$ ), the posterior distribution of  $Q_o$  derived by the HUP  
 167 method is as follows.

$$p(Q_o|Q_{f,i}, Q_b) = \frac{p(Q_{f,i}|Q_o, Q_b) \cdot p(Q_o|Q_b)}{\int_{-\infty}^{+\infty} p(Q_{f,i}|Q_o, Q_b) \cdot p(Q_o|Q_b) dQ_o} \quad (3)$$

168 where,  $p(Q_o|Q_b)$  is the prior density function,  $p(Q_{f,i}|Q_o, Q_b)$  is the likelihood density function.  $p(Q_o|Q_{f,i}, Q_b)$  is the posterior  
 169 density function.

170 The HUP method assumes that flow series transformed to normal space obey the Gaussian distribution. The cumulative  
 171 distribution function is different for forecasted and observed flows. The common normal quantile transformation is key to  
 172 the application of the HUP method, which its significance is to make the HUP method applicable to variables with any  
 173 marginal distributions, heteroskedasticity, and nonlinear dependence structures (Krzysztofowicz and Kelly, 2000;  
 174 Darbandsari and Coulibaly, 2021).

$$\hat{Q}_o = N^{-1}(P(Q_o)), \hat{Q}_{f,i} = N^{-1}(P(Q_{f,i})) \quad (4)$$

175 where,  $P(\cdot)$  denotes the probability distribution function.  $N^{-1}(\cdot)$  denotes the inverse function of the standard normal  
 176 distribution.  $\hat{Q}_o$  and  $\hat{Q}_{f,i}$  are the observed and forecasted flow transformed to the normal space, respectively.

177 The HUP method also assumes that the observed flow obeys the strictly stationary first-order Markov process  
 178 (Krzysztofowicz and Kelly, 2000), i.e., the flows between adjacent forecast horizons obey the linear constraint after the  
 179 normal transformation.

$$\hat{Q}_{o,t} = c_t \times \hat{Q}_{o,t-1} + \varepsilon_t \quad (5)$$

180 where,  $\hat{Q}_{o,t}$  is the observed flow corresponding to the  $t$ -th forecast horizon.  $c$  is the regression coefficient.  $\varepsilon$  is the residual,  
 181 obeying  $N(0, 1-c_t^2)$ .

182 The prior density function expressions are as follows.

$$p(\hat{Q}_{o,t}|\hat{Q}_b) = \frac{1}{(1-c_t^2)^{0.5}} n\left\{\frac{\hat{Q}_{o,t} - c_t \times \hat{Q}_b}{(1-c_t^2)^{0.5}}\right\}, c_t = \prod_{i=1}^t c_i \quad (6)$$

183 where,  $n(\cdot)$  denotes standard normal density function;  $\hat{Q}_b$  is the observed flow at the start of the forecast transformed to the  
 184 normal space.

185  $\hat{Q}_b$ ,  $\hat{Q}_o$ , and  $\hat{Q}_{f,i}$  are assumed to obey a linear relationship. The expression of the likelihood function in normal space is  
 186 as follows.

$$\hat{Q}_{f,i,t} = a_t \times \hat{Q}_{o,t} + d_t \times \hat{Q}_b + b_t + \theta_t$$

$$p(\hat{Q}_{f,i,t}|\hat{Q}_{o,t}, \hat{Q}_b) = \frac{1}{\sigma_t} n\left\{\frac{\hat{Q}_{f,i,t} - (a_t \times \hat{Q}_{o,t} + d_t \times \hat{Q}_b + b_t)}{\sigma_t}\right\} \quad (7)$$

187 where,  $\theta_t$  is an independent variable obeying  $N(0, \sigma_t^2)$ .  $a_t$ ,  $d_t$ , and  $b_t$  are regression coefficients.

188 The posterior density function under normal space can be derived by substituting Eqs. (6) and (7) into Eq. (3).

$$p(\hat{Q}_{o,t} | \hat{Q}_{f,i,t}, \hat{Q}_b) = \frac{1}{Y_t} n \left\{ \frac{\hat{Q}_{o,t} - (A_t \times \hat{Q}_{f,i,t} + D_t \times \hat{Q}_b + B_t)}{Y_t} \right\}, \quad (8)$$

$$A_t = \frac{a_t y_t^2}{a_t^2 y_t^2 + \sigma_t^2}, B_t = \frac{-a_t b_t y_t^2}{a_t^2 y_t^2 + \sigma_t^2}, D_t = \frac{C_t \sigma_t^2 - a_t d_t y_t^2}{a_t^2 y_t^2 + \sigma_t^2}, Y_t = \left( \frac{y_t^2 \sigma_t^2}{a_t^2 y_t^2 + \sigma_t^2} \right)^{0.5}, y_t^2 = 1 - C_t^2$$

189 The posterior distribution function under the normal space can be converted to the original space by Jacobian  
190 transformation (Liu et al., 2016). The posterior density function of  $Q_{o,t}$  under  $Q_{f,i,t}$  and  $Q_b$  conditions is as follows.

$$p(Q_{o,t} | Q_{f,i,t}, Q_b) = \frac{J(Q_{o,t})}{Y_t} n \left\{ \frac{N^{-1}(P(Q_{o,t})) - A_t N^{-1}(P(Q_{f,i,t})) - D_t N^{-1}(P(Q_b)) - B_t}{Y_t} \right\}, \quad (9)$$

$$J(Q_{o,t}) = \frac{p(Q_{o,t})}{n(N^{-1}(P(Q_{o,t})))}$$

191 where,  $J(\cdot)$  is the Jacobian transformation function.

### 192 3.1.3 HUP-BMA method

193 Darbandsari and Coulibaly et al. (2021) applied the hydrological uncertainty processor (HUP) to the ensemble forecast  
194 members, substituted the posterior density function obtained by the HUP method (Eq. (9)) into the BMA framework (Eq.  
195 (2)), and then obtained the posterior distribution function of the target flow based on the initial state and the forecasted flow  
196 of the ensemble member. Therefore, the expression of the HUP-BMA method is as follows.

$$p(Q_o | Q_{f,1}, Q_{f,2}, \dots, Q_{f,k}, Q_b) = \sum_{i=1}^k w_i \cdot \frac{J(Q_{o,t})}{Y_t} n \left\{ \frac{N^{-1}(P(Q_{o,t})) - A_t N^{-1}(P(Q_{f,i,t})) - D_t N^{-1}(P(Q_b)) - B_t}{Y_t} \right\} \quad (10)$$

### 197 3.1.4 Copula-based HUP-BMA (CHUP-BMA) method

#### 198 (1) Copula-based HUP

199 According to Sklar's theorem (Sklar, 1959), the joint distribution of  $m$  variables is as follows.

$$P(x_1, x_2, \dots, x_m) = C_m(P(x_1), P(x_2), \dots, P(x_m)) \quad (11)$$

200 where,  $C_m(\cdot)$  denotes the  $m$ -dimensional copula distribution.

201 The copula-based HUP method (CHUP) was proposed by Liu et al. (2018), which can avoid the normal quantile  
202 transformation process of the flow series in the standard HUP method. With the help of the copula function, the prior density  
203 function in Eq. (3) can be derived as follows.

$$p(Q_o | Q_b) = \frac{\partial^2 C_2(P(Q_o), P(Q_b))}{\partial P(Q_o) \partial P(Q_b)} \cdot \frac{dP(Q_o)}{dQ_o} = c_2(P(Q_o), P(Q_b)) \cdot p(Q_o) \quad (12)$$



204 where,  $c_m(\cdot)$  denotes the  $m$ -dimensional copula density function.  $m$  denotes the dimension.

205 The likelihood density function in Eq. (3) can be derived as follows.

$$p(Q_{f,i}|Q_o, Q_b) = \frac{\frac{\partial^3 c_3(P(Q_o), P(Q_{f,i}), P(Q_b))}{\partial P(Q_o) \cdot \partial P(Q_{f,i}) \cdot \partial P(Q_b)} \cdot dP(Q_{f,i})}{\frac{\partial^2 c_2(P(Q_o), P(Q_b))}{\partial P(Q_o) \cdot \partial P(Q_b)}} = \frac{c_3(P(Q_o), P(Q_{f,i}), P(Q_b))}{c_2(P(Q_o), P(Q_b))} \cdot p(Q_{f,i}) \quad (13)$$

206 The posterior density function in Eq. (3) can be derived as follows.

$$p(Q_o|Q_{f,i}, Q_b) = \frac{c_3(P(Q_o), P(Q_{f,i}), P(Q_b))}{\int_0^1 c_3(P(Q_o), P(Q_{f,i}), P(Q_b)) dP(Q_o)} \cdot p(Q_o) \quad (14)$$

## 207 (2) Copula-based HUP-BMA method

208 Applying CHUP to the  $i$ -th ensemble member, the posterior probability distribution function  $p(Q_o|Q_{f,i}, Q_b)$  of  $Q_o$  based  
 209 on  $Q_{f,i}$  and  $Q_b$  can be obtained. Coupling  $p(Q_o|Q_{f,i}, Q_b)$  into the BMA framework, the copula-based HUP-BMA (CHUP-  
 210 BMA) method can be constructed, and Eq. (2) can become as follows.

$$p(Q_o|Q_{f,1}, Q_{f,2}, \dots, Q_{f,k}, Q_b) = \sum_{i=1}^k w_i \cdot \frac{c_3(P(Q_o), P(Q_{f,i}), P(Q_b))}{\int_0^1 c_3(P(Q_o), P(Q_{f,i}), P(Q_b)) dP(Q_o)} \cdot p(Q_o) \quad (15)$$

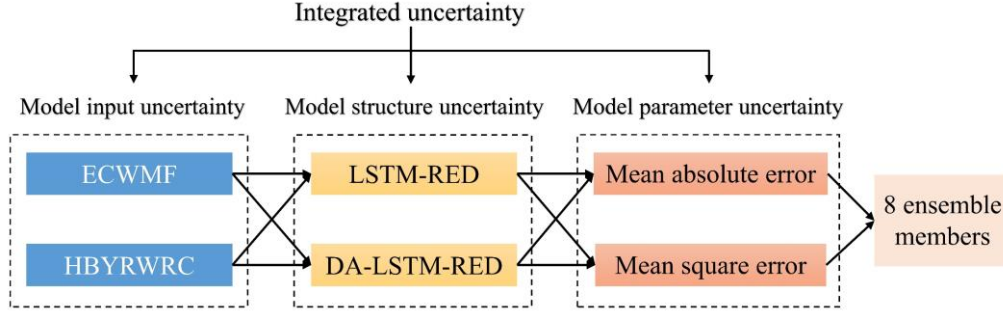
211 The forecast uncertainty is quantified by the forecast interval with a 90% confidence level. Before constructing the  
 212 copula, selecting the marginal distribution and the copula type is usually necessary. This study intends to select the  
 213 appropriate marginal distribution and copula function from five common distribution functions, such as Pearson type III (P-  
 214 III), Gamma, Normal, Lognormal, and Weibull, and five common copula functions, such as Gumbel-Hougaard, Frank,  
 215 Clayton, Student-t (Student) and Gaussian copula, according to the root mean square error (RMSE) minimization criterion,  
 216 respectively. The definition and mathematical expressions of copula functions can be referred to Liu et al. (2018) and Chen  
 217 and Guo (2019).

218 Darbandsari and Coulibaly (2021) demonstrated that the HUP-BMA method could improve the probabilistic forecasting  
 219 performance of the HUP and BMA methods in the short forecast horizons. Therefore, this paper focuses on analyzing and  
 220 comparing the performance of the HUP-BMA and CHUP-BMA methods. The HUP-BMA and CHUP-BMA methods only  
 221 calibrate the ensemble members' weights through the Expectation-Maximization (EM) algorithm (Darbandsari and  
 222 Coulibaly, 2021). Meanwhile, since the forecast accuracy of ensemble members may change with time due to seasonality  
 223 and other factors (Zhong et al., 2020), the sliding window approach is used to update the weighting parameters. Parrish et al.  
 224 (2012) and Darbandsari and Coulibaly (2019) have shown that the BMA method with the sliding window can obtain better  
 225 probabilistic forecast performance compared to the method without the sliding window.

## 226 3.2 Ensemble forecasting scheme

227 An ensemble forecast scheme containing multi-source uncertainties in the model input, the model structure, and the  
 228 parameter is constructed using a multi-member approach consisting of two forecasted precipitation, two models, and two  
 229 objective functions used to calibrate parameters, as shown in Fig. 2.

230



231

232

233

Fig. 2 The TGR's flood ensemble forecast scheme

### 234 3.2.1 Model input uncertainty

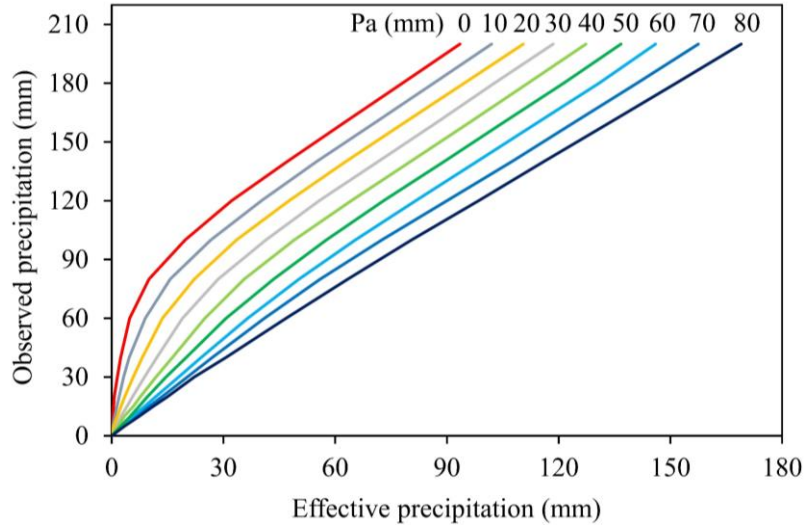
235 There are five flow discharge inputs from five large tributaries (Jinsha, Min, Jialing, Tuo, and Wu Rivers) in our case  
 236 study. The flow discharges are observed at the Pingshan, Gaochang, Fushun, Beibei, and Wulong hydrological controlled  
 237 stations, respectively. Since these observed (or forecasted) flows are respectively regulated by their upstream cascade  
 238 reservoirs, these flow data inputs are more accurate than the rainfall inputs. This study collected the forecasted precipitation  
 239 data from the European Centre for Medium-Range Weather Forecasts (ECMWF) and HBYRWRC in these three sub-basins.  
 240 Since the rainfall data is more diverse and has relatively large uncertainty, the forecast rainfall input variable is used to  
 241 explore the impact of forecast rainfall uncertainty on the TGR inflow forecasts. The TGR is a river-type reservoir, so  
 242 building a river confluence model for flood forecasting is necessary. The observed and forecasted precipitations are  
 243 converted into the effective precipitation in the three sub-basin areas, which accounts for the losses of plant reception,  
 244 infiltration, evaporation, etc. The rainfall-runoff relationship (Fedora and Beschta, 1989) commonly used in the Yangtze  
 245 River basin to calculate the effective precipitation. The antecedent precipitation index, which is the key variable of the  
 246 method, can be calculated by the following equation to represent the soil moisture content (Zhong et al., 2018b).

$$P_{a,t+1} = k(P_{a,t} + P_t) \quad (16)$$

$$P_{a,t+1} \leq I_m \quad (17)$$

247 where  $P_{a,t}$  denotes the antecedent precipitation index on the  $t$ -th day,  $P_t$  is the daily precipitation,  $I_m$  is the water storage  
 248 capacity of the basin,  $k$  denotes evaporation reduction index.

249 The values of  $k$  and  $I_m$  for these three sub-basins are listed in Table 2, which are obtained from the HBYRWRC. Since  
 250 the rainfall-runoff relationship graph method have been widely used for runoff generation calculation in the Yangtze River  
 251 basin, the rainfall-runoff relationship between Xiangjiaba and Three Gorges dam-site uncontrolled interval basin are  
 252 established and plotted in Fig. 3, which is used to calculate the effective precipitation based on the antecedent precipitation  
 253 index ( $P_a$ ) and observed (or forecasted) precipitation for these three sub-basins.  
 254



255  
 256 **Fig. 3** Rainfall-runoff relationship between Xiangjiaba and Three Gorges dam-site uncontrolled interval basin  
 257

258 **Table 2** The  $k$  and  $I_m$  values for the three sub-basin areas

Sub-basin	$k$	$I_m$
Pingshan-Cuntan	0.90	50
Cuntan-Wanxian	0.95	80
Wanxian-TGR dam-site	0.95	80

259  
 260 After obtaining the daily antecedent precipitation index at 8:00, the antecedent precipitation index for the 6-h time scale  
 261 is calculated as follows.

$$P_{a,t,m} = (P_{a,t} + \sum P_{t,n}) \times k^{\frac{h}{24}} \quad (18)$$

262 where,  $P_{a,t,m}$  denotes the antecedent precipitation index at  $m:00$  on the  $t$ -th day.  $\sum P_{t,n}$  denotes the cumulative observed  
 263 precipitation from 8:00 to  $m:00$  on the  $t$ -th day.  $h$  denotes the time gap from 8:00 to  $m:00$  on the  $t$ -th day.

### 264 3.2.2 Model structure uncertainty

265 The TGR inflow forecasting is influenced by the upstream mainstream and tributary reservoir scheduling decisions, the  
266 rainfall intensity and distribution in the interval basin, and the changes in the subsurface characteristics, which is challenging  
267 to establish complex and physical-based hydrological models (Yang et al., 2019; Cho et al., 2022; Hauswirth et al., 2023).  
268 The simulation or forecast accuracy in this interval-basin needs to be improved to meet the needs of the work. Therefore, two  
269 advanced data-driven models for obtaining multi-step-ahead flood processes forecasting, namely the long short-term  
270 memory (LSTM-RED) model based on an encoder-decoder structure and the coupled dual attention LSTM-RED (DA-  
271 LSTM-RED) model, are used for confluence calculations as a way to consider the uncertainty in the model structure. Since  
272 the forecast data series at the outlets of tributaries are inconsistent, the observed flow at the outlets of five large tributaries  
273 are used to train and validate the proposed models.

#### 274 (1) Long short-term memory model based on encoder-decoder structure

275 The structure of LSTM neural network includes forgetting gate, input gate, updating the state of the memory unit, and  
276 output gate (Hochreiter and Schmidhuber, 1997). The forgetting gate can select the relatively important information in the  
277 previous memory unit. The input gate can select useful information from the input variables at the current moment. The  
278 memory unit state can store relatively important information extracted from historical moments, which is updated under the  
279 control of the forgetting gate and the input gate. The output gate selects and outputs useful information from the memory cell  
280 state. More detailed procedures of the LSTM neural network formulation have been described by Kratzert et al. (2018).

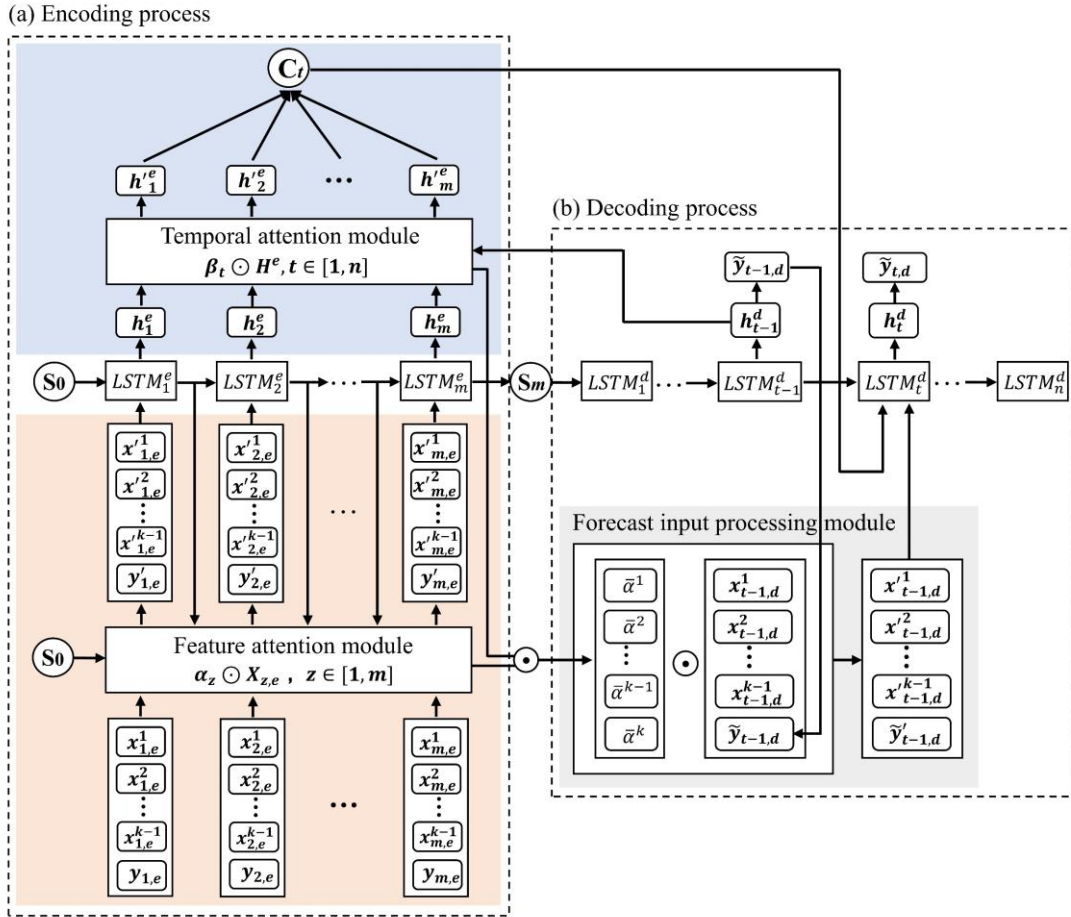
281 This study nests an LSTM neural network into a recursive encoder-decoder (RED) structure that can be obtained for  
282 forecasting flood processes to build an LSTM-RED model. Among them, the RED structure is similar to that of Kao et al.  
283 (2020). The description of the LSTM neural network can be found in Cui et al. (2022). The encoding process of the RED  
284 structure is used to extract the critical information ( $C_t$ ) of the input (Xiang et al., 2020). In the decoding process, forecast  
285 information of the same category as the encoding process is input to the neural network of the latter moment, besides the  $C_t$   
286 and the output of the hidden layer at the previous moment.

#### 287 (2) LSTM-RED neural network coupled dual attention mechanism

288 The LSTM-RED model based on the dual attention mechanism (DA-LSTM-RED) is established by adding the feature-  
289 temporal dual attention mechanism to the LSTM-RED model, which can enable the model to highlight effective information  
290 in different types and moments of the input. The DA mechanism (Fig. 4) consists of the feature attention module, the  
291 temporal attention module, and the forecast input processing module.

292 The feature attention module can adaptively highlight the critical input types by assigning feature weights to the input  
293 of the encoding process (Qin et al., 2017). The temporal attention module can highlight the information (hidden layer states)  
294 extracted at critical time step by assigning temporal weights to the information extracted at all time step in the encoding  
295 process (Ding et al., 2020). Meanwhile, the feature weights are averaged based on temporal weights and applied them to the

296 forecast information inputted in the decoding process, thus highlighting the key forecast input variables. The principle of the  
 297 DA-LSTM-RED model can be found in Cui et al. (2023).  
 298



299  
 300 **Fig. 4** Schematic diagram of the DA-LSTM-RED model.  $e$  and  $d$  are the encoding and decoding processes, respectively.  $k$  is the number of  
 301 input types.  $X_{z,e}$  is the input variable of encoding process,  $X_{z,e} = \{x_{z,e}^1, x_{z,e}^2, \dots, x_{z,e}^{k-1}, y_{z,e}\}$ .  $\alpha_z$  denotes the weights of the input variables,  
 302  $\alpha_z = \{\alpha_z^1, \alpha_z^2, \dots, \alpha_z^k\}$ .  $m$  is the input time-steps in the encoding process.  $S$  is the hidden layer output.  $n$  is the maximum forecast horizon.  $H^e$   
 303 is the hidden layer state,  $H^e = \{h_1^e, h_2^e, \dots, h_m^e\}$ .  $\beta_t$  denotes the weights of the hidden layer states of the encoding process,  $\beta_t = \{\beta_t^1, \beta_t^2, \dots, \beta_t^m\}$ .  
 304  $C$  denotes the key information highlighted by the temporal attention.  $\bar{\alpha}$  denotes the forecast input weights.

305

### 306 (3) Model input and hyperparameter selection

307 In this study, the input types for the encoding process include effective precipitation in the three sub-basins, flow  
 308 discharge in the mainstream and tributaries (i.e., five hydrological stations in Table 1), and previously observed inflow to the  
 309 TGR for a total of nine data types. In order to make the model learn comprehensive information, input variables with the last

310 11-time steps (66h) are inputted to the encoding process according to the flow propagation times from the hydrological  
311 stations to the TGR dam site in Table 1.

312 The forecasted effective precipitation, the forecasted flow of the mainstream and tributaries, and the forecasted flow for  
313 the previous forecast horizon are used as inputs of the decoding process. Among them, the forecasted effective precipitation  
314 is calculated by the observed precipitation during the training period and by the forecast precipitation during the validation  
315 period. The forecasted flow of the upstream mainstream and tributaries is replaced by the observed flow during the training  
316 and validation periods. The TGR's observed inflow for the 6-168h forecast horizons is the target output, needed for practical  
317 forecasting.

318 The input and output data are handled by the normalization method. Moreover, the trial-and-error method is used for  
319 debugging the network hyperparameters. The model is trained by the Adam method (Kingma& Ba, 2014).

### 320 3.2.3 Model parameter uncertainty

321 Different parameter-optimization objective functions may focus on different forecast results (Zhong et al., 2020). For  
322 example, the mean absolute error function focuses on the magnitude of the error mean. The mean square error function  
323 usually is sensitive to outliers with large errors, which may make the model parameters with different objective functions  
324 produce forecast results with different focus points (Duan et al., 2007). Therefore, it is necessary to consider the uncertainty  
325 of the model parameters. Neural network models usually train model parameters (such as model internal weights and bias  
326 values, etc.) based on loss functions, so this paper uses two common loss functions, namely the mean absolute error and the  
327 mean square error, to train the model as a way to consider the uncertainty of model parameters.

## 328 3.3 Evaluation metrics

### 329 3.3.1 Deterministic forecast evaluation metrics

330 The accuracy of deterministic forecast is evaluated by three metrics: the Nash-Sutcliffe efficiency (Nash and Sutcliffe,  
331 1970) (NSE), the mean absolute error (MAE) and the relative error of total runoff (RE).

$$NSE = 1 - \frac{\sum_{i=1}^N (Q_{o,i} - Q_{f,i})^2}{\sum_{i=1}^N (Q_{o,i} - \overline{Q_o})^2} \quad (19)$$

$$RE = \frac{\sum_{i=1}^N Q_{f,i} - \sum_{i=1}^N Q_{o,i}}{\sum_{i=1}^N Q_{o,i}} \times 100\% \quad (20)$$

$$MAE = \frac{1}{N} \sum_{i=1}^N |Q_{o,i} - Q_{f,i}| \quad (21)$$

332 where,  $N$  is the sample number.  $\overline{Q_o}$  and  $\overline{Q_f}$  are the average of the observed and forecasted flow, respectively.

333 The Nash-Sutcliffe efficiency (NSE) is one of the most important metrics in flood forecasting, reflecting the degree of  
334 fit between forecasted and observed flows (Nash & Sutcliffe, 1970). Since the accurate runoff volume predictions is more

335 important than peak discharge for the operation of a large reservoir (Cui et al., 2023), the relative error for total runoff  
 336 volume (RE) is also chosen. The mean absolute error (MAE) can reflect the forecast error for each moment, and compared  
 337 with the continuous ranked probability score (CRPS) of the ensemble forecast (Raftery et al., 2005), which can reflect the  
 338 effectiveness of the ensemble forecast correction.

### 339 3.3.2 Probabilistic forecast evaluation metrics

#### 340 (1) Forecast interval evaluation metrics

341 The forecast interval is evaluated by three metrics: the average coverage rate (CR), average interval width (IW), and the  
 342 percentage of observations bracketed by the unit confidence Interval (PUCI) (Li et al., 2011).

$$CR = \frac{n_c}{N} \quad (22)$$

$$IW = \frac{1}{N} \sum_{i=1}^N (Q_{u,i} - Q_{l,i}) \quad (23)$$

$$PUCI = \frac{CR}{\frac{1}{N} \sum_{i=1}^N \left( \frac{Q_{u,i} - Q_{l,i}}{Q_{o,i}} \right)} \quad (24)$$

343 where,  $n_c$  denotes the number of  $Q_o$  located in the forecast interval.  $Q_u$  and  $Q_l$  are the upper and lower boundaries of the  
 344 forecast interval with a 90% confidence level, respectively.

345 The average coverage rate (CR) is one of the most necessary metrics for evaluating the reliability of forecast intervals  
 346 (Li et al., 2021). The average interval width (IW) is the metric that directly reflects the level of forecast uncertainty, which is  
 347 an important metric for evaluating the effectiveness of the proposed methods. The percentage of observations bracketed by  
 348 the unit confidence Interval (PUCI) is a comprehensive metric for evaluating the performance of forecast intervals in  
 349 quantifying uncertainty (Xiong et al., 2009). Therefore, the CR, RB, and PUCI metrics are selected to evaluate the forecast  
 350 intervals performance.

#### 351 (2) Probabilistic forecast evaluation metrics

352 The probabilistic forecast is evaluated by three metrics: the  $\alpha$ \_index (Renard et al., 2010), the ignorance score (IGS)  
 353 (Gneiting et al., 2005), and continuous ranked probability score (CRPS) (Raftery et al., 2005).

$$\alpha\_index = 1 - \frac{2}{N} \sum_{i=1}^N |q_{e,i} - q_{th,i}| \quad (25)$$

$$IGS = -\frac{1}{N} \sum_{i=1}^N \ln(p(Q_{o,i})) \quad (26)$$

$$CRPS = \frac{1}{N} \sum_{i=1}^N \int_0^{+\infty} (P_i(r) - I(r - Q_{o,i}))^2 dr, \quad (27)$$

$$I(r - Q_{o,i}) = \begin{cases} 1 & r \geq Q_{o,i} \\ 0 & r < Q_{o,i} \end{cases}$$

354 where,  $q_{e,i}$  and  $q_{th,i}$  denote observed and theoretical p-values of  $Q_{o,i}$ , respectively. p-value denotes the posterior probability  
 355 distribution value of the  $Q_{o,i}$  (Renard et al., 2010).  $I(\cdot)$  denotes the indicator function.  $r$  denotes the flow variable.

356 The  $\alpha$ \_index metric can quantitatively assess the reliability of ensemble probabilistic forecasts from the perspective of  
 357 distribution function values (Renard et al., 2010). The closer the  $\alpha$ \_index value is to 1, the more reliable the probabilistic  
 358 forecast is. The IGS and CRPS metrics can reflect the reliability and sharpness of the probabilistic forecast. The former can  
 359 quantify the forecast probability density at the observation, while the latter can indicate the fit performance between the  
 360 posterior probabilistic distribution and the actual probabilistic distribution of  $Q_o$  (Raftery et al., 2005). Both CRPS and IGS  
 361 are negative scores, i.e., the smaller the value, the better. The IGS imposes severe penalties for particularly poor probabilistic  
 362 predictions and may be extremely sensitive to outliers and extreme events, yet also lacks robustness (Raftery et al., 2005).

## 363 **4 Results evaluation**

### 364 **4.1 Deterministic forecast results of ensemble member**

365 Since the study focuses on the differences in ensemble forecast performance between the HUP-BMA and CHUP-BMA  
 366 methods, the overall forecast accuracy of members is analysed (Fig. 5), and the differences in forecast accuracy between  
 367 members are not explicitly analysed. As shown in Fig. 5, using the observed values as input during the training period, high  
 368 forecast accuracy can be acquired in different forecast horizons, with the NSE values exceeding 0.95 and the MAE values  
 369 below 1400 m<sup>3</sup>/s, and the absolute value of RE within 4%.

370 After combining the forecasted precipitation during the validation period, the NSE values show a decreasing trend, and  
 371 the MAE and RE values show an increasing trend with the increase of the forecast horizon. Taking the NSE metrics of the 1-  
 372 7d forecast horizons as an example (Table 3), the average value of the NSE metric decreases from 0.97 to 0.89, which  
 373 indicates that the forecast accuracy gradually decreases. Meanwhile, the range of evaluation metrics gradually increases with  
 374 the increase of the forecast horizon. It can be seen from Table 3 that the difference between the maximum and minimum  
 375 values of NSE indicators for the 1d forecast horizon is only 0.01. In contrast, the difference for the 7d forecast horizon is as  
 376 high as 0.05, which indicates that the difference in forecast accuracy of members is also more significant, and the forecast  
 377 uncertainty gradually increases. Overall, the NSE values of the forecast members in the 6-168h forecast horizons are higher  
 378 than 0.88, and the absolute values of the RE metrics are within 7%. Hence, the forecast accuracy of members is relatively  
 379 high, and the forecast error is low, which can be used for flood ensemble forecasting.

380

381



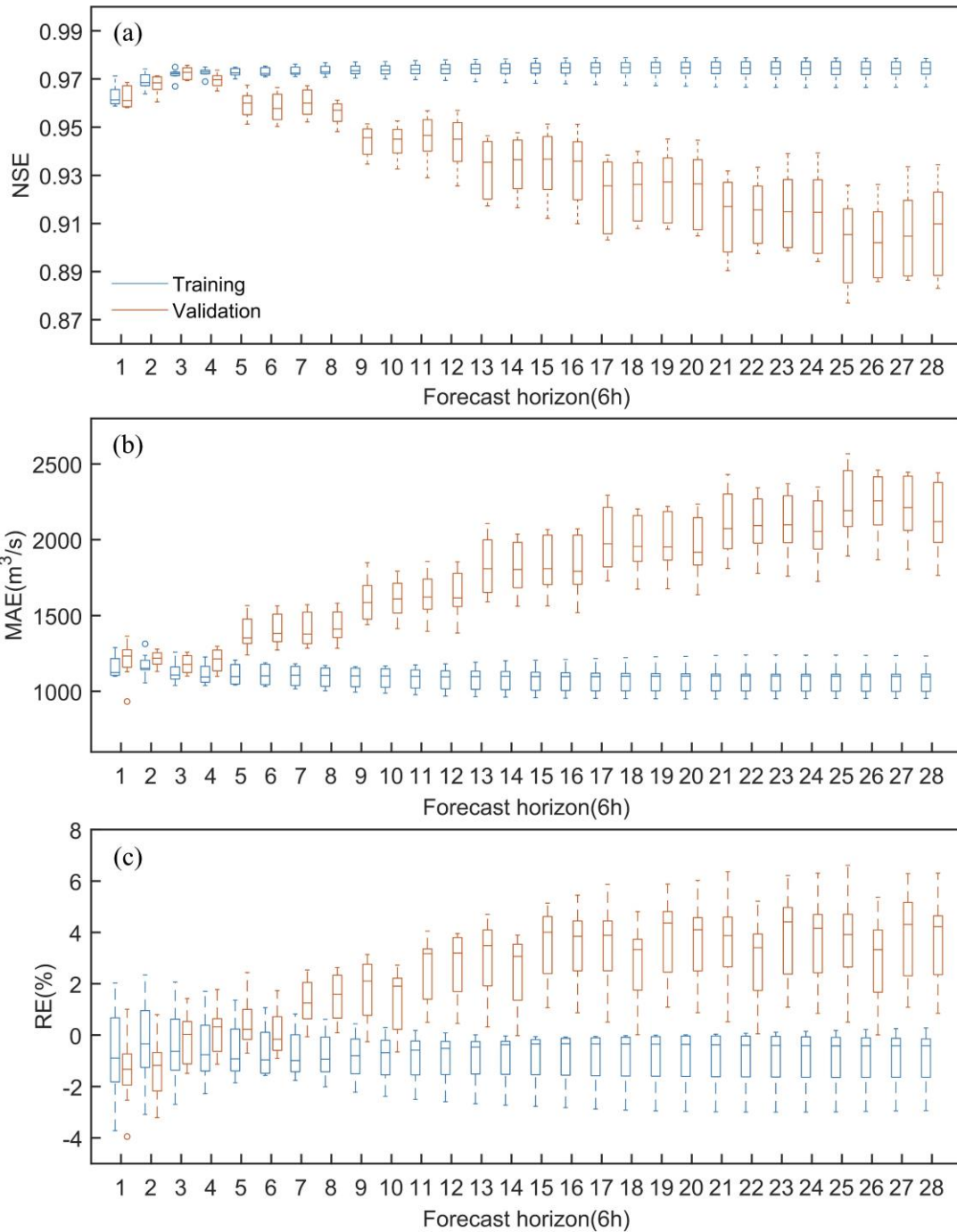


**Fig. 5** Statistical chart of evaluation metrics of 8 ensemble members

382  
 383  
 384  
 385

**Table 3** Mean, minimum, and maximum values of NSE metrics for 8 ensemble members in the validation period

Forecast horizon (h)	Mean	Max	Min	Forecast horizon (h)	Mean	Max	Min
6	0.96	0.97	0.96	90	0.93	0.95	0.91
12	0.97	0.97	0.96	96	0.93	0.95	0.91
18	0.97	0.98	0.97	102	0.92	0.94	0.90
24	0.97	0.97	0.97	108	0.92	0.94	0.91
30	0.96	0.97	0.95	114	0.93	0.95	0.91
36	0.96	0.97	0.95	120	0.92	0.94	0.90
42	0.96	0.97	0.95	126	0.91	0.93	0.89
48	0.96	0.96	0.95	132	0.91	0.93	0.90
54	0.94	0.95	0.93	138	0.92	0.94	0.90
60	0.94	0.95	0.93	144	0.91	0.94	0.89
66	0.95	0.96	0.93	150	0.90	0.93	0.88
72	0.94	0.96	0.93	156	0.90	0.93	0.89
78	0.93	0.95	0.92	162	0.91	0.93	0.89
84	0.93	0.95	0.92	168	0.91	0.93	0.88

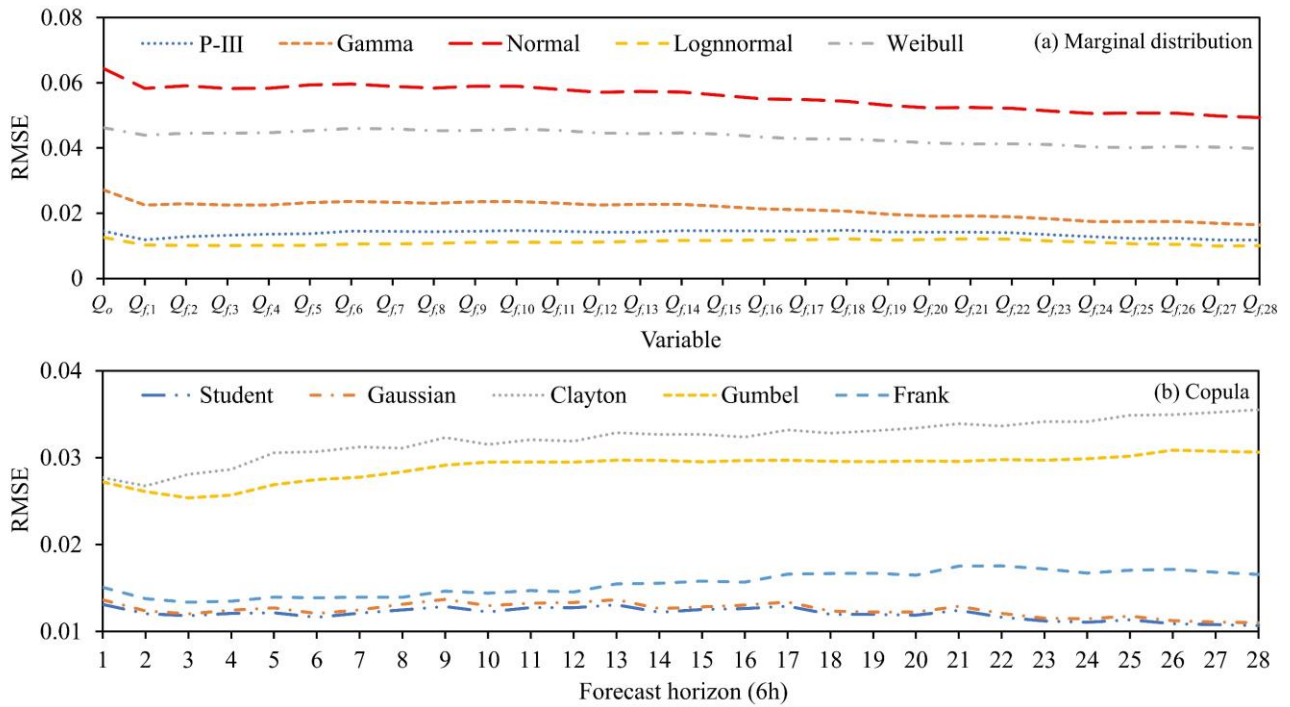
387

388 **4.2 Ensemble forecast results**389 **4.2.1 Marginal distribution and copula function selection**

390 It is necessary first to fit the marginal distributions of the observed flow and the forecasted flow of the 6~168h forecast  
391 horizons. The  $Q_o$  and  $Q_b$  obey the same distribution. The RMSE criterion is used to select the marginal distribution type. In  
392 each forecast horizon, the RMSE values of the 8 members are averaged to obtain the marginal distribution suitable for the  
393 forecasted flow intuitively. Meanwhile, according to Eq.(14), the three-dimensional joint distribution of  $Q_o$ ,  $Q_b$ , and  $Q_f$  needs  
394 to be constructed. The RMSE criterion is used to select the copula function. Similarly, the RMSE values for the 8 members  
395 of each forecast horizon were averaged.

396 Figs.6(a) and (b) show the RMSE values generated by fitting the marginal distribution and copula function, respectively.  
397 It can be seen from Fig. 6(a) that the Lognormal distribution has the lowest RMSE value among the five alternative marginal  
398 distributions and is chosen as the sequence marginal distribution type. As shown in Fig.6(b), the student copula has the  
399 lowest RMSE value in the 6-168h forecast horizons and is chosen to construct the three-dimensional joint distribution  
400 function of  $Q_o$ ,  $Q_b$ , and  $Q_f$ .

401



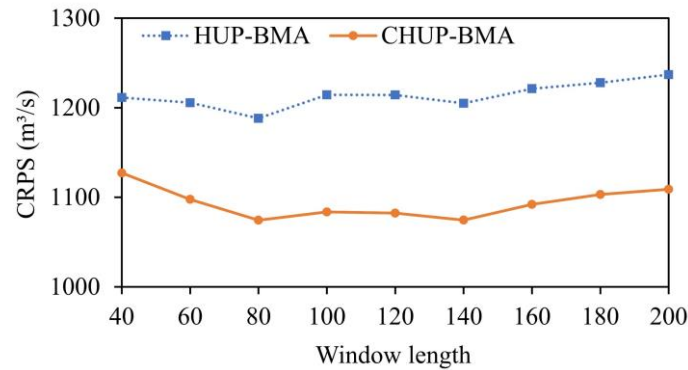
402

403 **Fig. 6** The RMSE values of  $Q_o$ ,  $Q_b$  and  $Q_f$  sequence marginal distributions and copula functions. 1, 2, ..., 28 denote 6h, 12h, ..., 168h  
 404 forecast horizons, respectively.

405 **4.2.2 Sliding window length selection**

406 Since there is no specific method or rule to calculate the sliding window length, this study adopts the CRPS metric as  
 407 the objective function and the trial-and-error method to select the sliding window length. The range of window lengths is [40,  
 408 200].

409



410

411 **Fig. 7** The average CRPS values of the CHUP-BMA and HUP-BMA methods with different window lengths

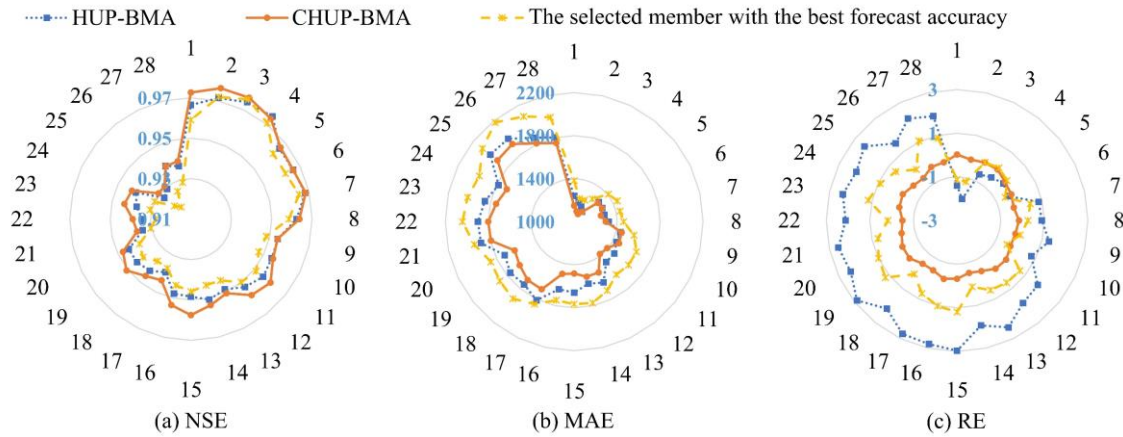
412

413 To facilitate the selection of the sliding window lengths, Fig. 7 shows the average CRPS values of the HUP-BMA and  
 414 CHUP-BMA methods for all forecast horizons with different window lengths. It can be seen from Fig. 7 that the HUP-BMA  
 415 and CHUP-BMA methods all have the lowest CRPS values at the sliding window length of 80. Therefore, 80 is the optimal  
 416 window length for the ensemble forecasting study.

#### 417 4.2.3 Deterministic forecast results of ensemble forecast

418 The HUP-BMA and CHUP-BMA methods use **expected** values of ensemble forecasts as deterministic forecast results.  
 419 In order to analyze the deterministic forecast performance of ensemble forecasts, one member with the best forecast accuracy  
 420 is selected for comparative analysis based on the criteria of the relatively low RE and MAE values and relatively high NSE  
 421 values, which is composed of the forecast rainfall from ECWMF, the DA-LSTM-RED model, and the objective  
 422 function with mean square error to optimize the parameters.

423



424

425 **Fig. 8** Deterministic forecast evaluation metrics for the HUP-BMA, the CHUP-BMA, and the selected member with the best forecast  
 426 accuracy

427

428 Fig.8(a), (b), and (c) show the NSE, MAE, and RE metrics of three deterministic forecast results, respectively. It can be  
 429 seen that the NSE metrics show a decreasing trend, and the MAE metrics show an increasing trend as the forecast horizon  
 430 increases, indicating a gradual decrease in forecast accuracy.

431 As shown in Fig. 8(a), the NSE metrics of three forecast results are at least 0.92 during the 6-168h forecast horizons.  
 432 The difference between the two is small, not more than 0.02. Among them, the CHUP-BMA method has the best NSE  
 433 metrics. However, the advantage value gradually decreases as the forecast horizon increases. The NSE metrics of the HUP-  
 434 BMA method are better than those of the selected forecast member in most forecast horizons. From Fig.8(b), the maximum  
 435 and mean values of MAE are 1923 and 1513 m<sup>3</sup>/s for the CHUP-BMA method, 1999 and 1582 m<sup>3</sup>/s for the HUP-BMA  
 436 method, and 2179 and 1719 m<sup>3</sup>/s for the selected forecast member, respectively. The CHUP-BMA method has the best MAE

437 metric, with the maximum and average reduction of 10.69% and 4.36% relative to the HUP-BMA method, respectively.  
 438 Meanwhile, the MAE values of two ensemble forecasting methods are lower than those of the selected forecast members. As  
 439 shown in Fig.8(c), the maximum and mean of the RE metric are 0.02% and -0.27% for the CHUP-BMA method, 2.97% and  
 440 1.36% for the HUP-BMA method, and 1.20% and 0.34% for the selected forecast member, respectively. The CHUP-BMA  
 441 method can reduce the RE metrics of the selected forecast member in most forecast horizons, while the HUP-BMA method  
 442 has no advantage in the RE metric. Overall, ensemble forecast methods can somewhat improve the selected best member  
 443 forecast accuracy. The CHUP-BMA method's expectation forecast has the best accuracy, which indicates that the copula-  
 444 based CHUP-BMA method can improve the performance of the HUP-BMA method in correcting errors.

445 To further analyze the accuracy of ensemble forecast methods, seven floods with peaks exceeding 50,000 m<sup>3</sup>/s during  
 446 the 24 and 168h forecast horizons in the validation period (2017-2021) are selected for analyzing. The average relative error  
 447 metric of peak (PRE) (Cui et al., 2022) is added to analyze the forecasting performance for flood peaks. Table 4  
 448 demonstrates the forecast evaluation metrics for the seven flood events. With the increase in the forecast horizon, the NSE  
 449 metric shows a decreasing trend, and the RE and MAE metrics show an increasing trend, indicating a gradual decrease in  
 450 forecasting performance. It can be seen from Table 4 that (1) in the 24h forecast horizon, the forecast accuracy of the two  
 451 methods is similar for most flood events and quality metrics, (2) in the 168h forecast horizon, the forecast accuracy of the  
 452 CHUP-BMA method is better than HUP-BMA method in most flood events and quality metrics. The average values of the  
 453 NSE, RE, MAE, and PRE are 0.88, -0.63%, 2980m<sup>3</sup>/s, and -4.55% for CHUP-BMA, and 0.84, -2.38%, 3188m<sup>3</sup>/s, and -6.46%  
 454 for HUP-BMA, respectively, indicating an overall improvement of CHUP-BMA over HUP-BMA in forecasting accuracy.

455

456

**Table 4** Evaluation metrics for forecast flood events for 24 and 168h forecast horizons

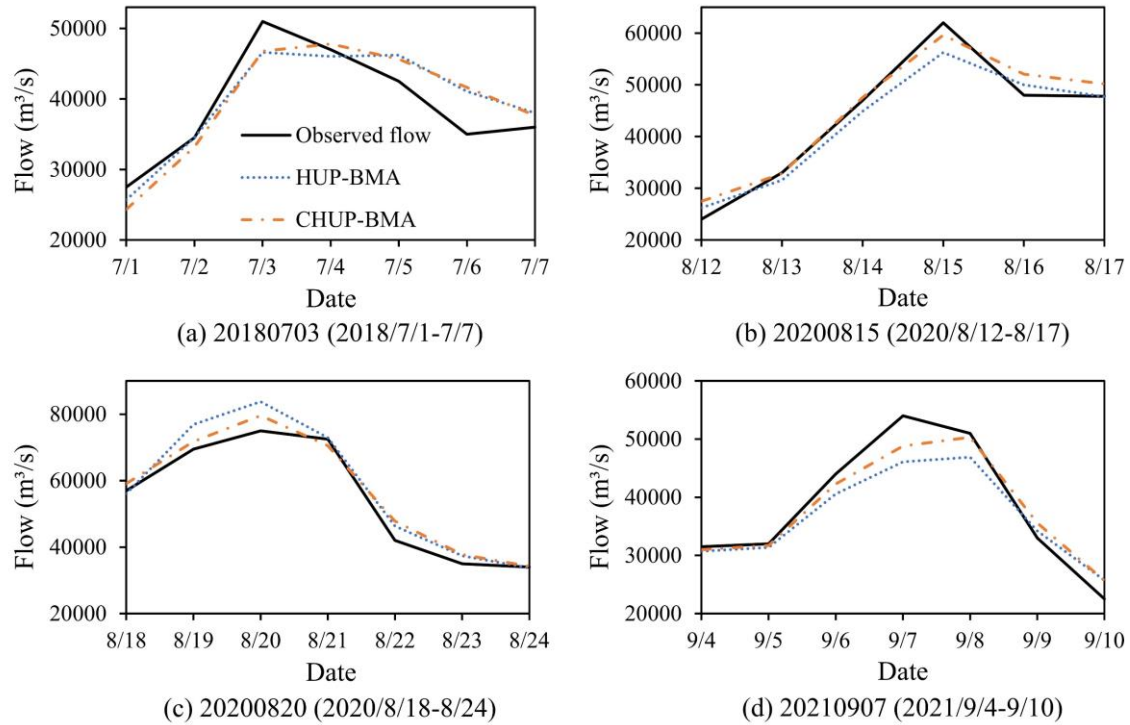
Flood event	Method	Forecast horizon (h)	Evaluation metric			
			NSE	RE (%)	MAE (m <sup>3</sup> /s)	PRE (%)
20180703 (2018/7/1-7/7)	HUP-BMA	24	0.93	1.95	1697	-3.29
		168	0.80	1.69	2709	-8.60
	CHUP-BMA	24	0.94	3.63	1667	1.64
		168	0.78	1.30	2988	-6.26
20180714 (2018/7/11-7/17)	HUP-BMA	24	0.85	-1.38	2768	-8.04
		168	0.97	0.11	1101	0.88
	CHUP-BMA	24	0.84	-1.97	2874	-7.70
		168	0.95	-2.37	1587	-1.23
20200717 (2020/7/14-7/20)	HUP-BMA	24	0.91	-7.02	3094	-10.02
		168	0.64	-11.67	5965	-19.00
	CHUP-BMA	24	0.91	-4.75	3211	-8.80
		168	0.75	-7.45	5255	-13.58

20200727 (2020/7/25-7/31)	HUP-BMA	24	0.97	-0.22	1371	0.02
		168	0.84	-4.73	3044	-13.47
	CHUP-BMA	24	0.94	4.40	1819	3.62
		168	0.88	0.04	3155	-7.79
20200815 (2020/8/12-8/17)	HUP-BMA	24	0.93	-1.31	2714	-8.21
		168	0.94	-1.96	2259	-9.25
	CHUP-BMA	24	0.96	2.06	2062	-3.53
		168	0.95	3.05	2167	-3.82
20200820 (2020/8/18-8/24)	HUP-BMA	24	0.95	-0.79	2772	0.22
		168	0.92	5.74	3509	11.72
	CHUP-BMA	24	0.96	2.58	2125	2.60
		168	0.96	4.08	2816	6.06
20210907 (2021/9/4-9/10)	HUP-BMA	24	0.94	-3.26	2231	-7.43
		168	0.87	-4.66	3042	-13.15
	CHUP-BMA	24	0.97	-0.64	1722	-4.07
		168	0.94	-0.99	2016	-6.82

457

458 To further demonstrate the accuracy of flood process forecasting and applicability of the two methods, four relatively  
459 large flood events are selected for comparative analysis for 168h forecast horizon (Fig.9). In the 20180703-flood event (Fig.  
460 9a), the two methods have similar forecast performance, underestimating the peak and rising water processes and  
461 overestimating the receding water process. The CHUP-BMA method has relatively low PRE values and total runoff error.  
462 The HUP-BMA method accurately forecasts the peak present time. In the 20200815-flood event (Fig.9b), two methods  
463 underestimate the flood peak and overestimate the receding water process. The HUP-BMA method has a larger flood peak  
464 error, and the CHUP-BMA method has a better fitting performance. In the 20200820-flood event (Fig.9c), two methods  
465 overestimate the observed flood process, with the CHUP-BMA method having the lower peak and total runoff error than the  
466 HUP-BMA method. In the 20210907-flood event (Fig.9d), the CHUP-BMA and HUP-BMA methods underestimate the  
467 flood peak and delay the forecast peak occurring time. The former has smaller peak and water volume error.

468



469  
470 **Fig. 9** Forecasted flood events during 168h forecast horizon for the HUP-BMA and the CHUP-BMA methods  
471

472 **4.2.4 Probabilistic forecast results of ensemble forecast**

473 **(1) Evaluation of forecast interval**

474 Figs. 10(a), (b), and (c) show the CR, IW, and PUCI metrics for the forecast interval with a 90% confidence level,  
475 respectively. Fig.10(a) shows that during the 6-168h forecasting period, the maximum, minimum, and mean of the CR metric  
476 for the forecast interval of the CHUP-BMA method are 0.92, 0.88, and 0.89, respectively, and 0.93, 0.88, and 0.91 for the  
477 HUP-BMA method, respectively. The CR values of the two methods' forecast intervals are close to or exceed the 90%  
478 confidence level, indicating that the forecast intervals are reliable.

479 It is obvious from Fig.10(b) that the forecast interval width tends to increase with the increase of the forecast horizon,  
480 indicating that the forecast uncertainty gradually increases. The maximum, minimum, and mean of the IW metrics for the  
481 forecast interval of the CHUP-BMA method are 7820, 3337, and 6257  $\text{m}^3/\text{s}$ , respectively, and 8888, 4662, and 7345  $\text{m}^3/\text{s}$  for  
482 the HUP-BMA method, respectively. The forecast intervals of the CHUP-BMA method are significantly narrower than those  
483 of the HUP-BMA method, with the maximum and average reduction of 28.42% and 15.32%, respectively, which indicates  
484 that the CHUP-BMA method can effectively reduce the interval width and forecast uncertainty.

485

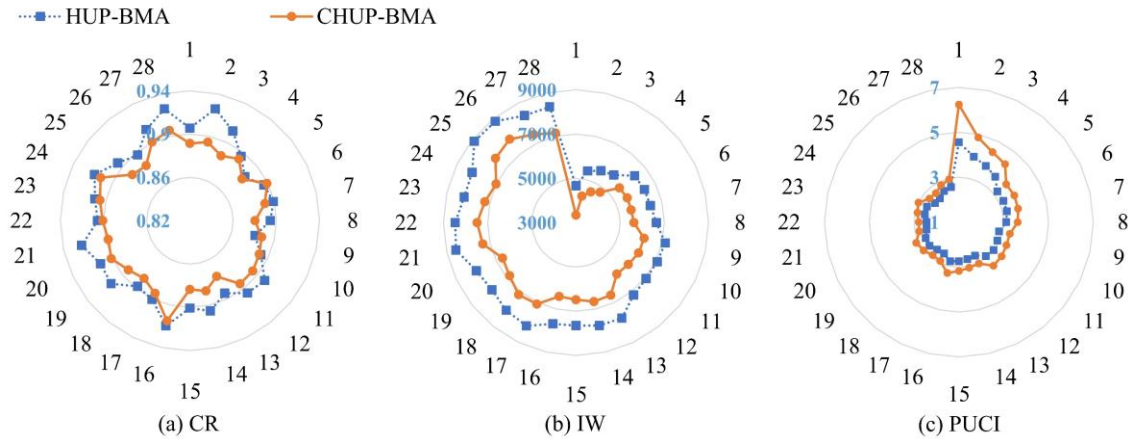


**Fig. 10** Evaluation metrics of forecast intervals with the 90% confidence level of the HUP-BMA and CHUP-BMA methods

From Fig.10(c), the maximum, minimum, and mean of the PUCI metric for the forecast interval of the CHUP-BMA method are 6.24, 2.65, and 3.48, respectively, and 4.55, 2.35, and 2.95 for the HUP-BMA method, respectively. The CHUP-BMA method has the higher PUCI values, indicating that the forecast interval of the CHUP-BMA method reflects the forecast uncertainty relatively well.

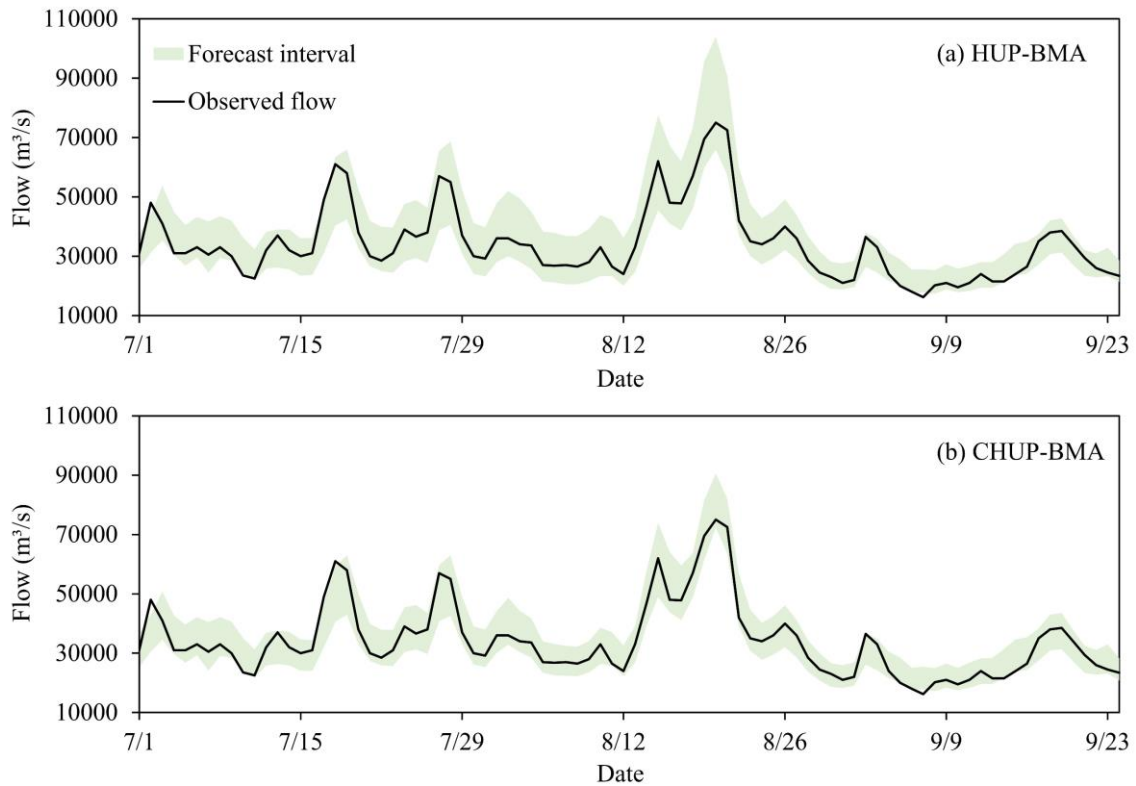
In summary, the CHUP-BMA outperforms the HUP-BMA method under the premise that the CR values are close to or exceed the 90% confidence level. The CHUP-BMA method has narrower forecast intervals and better performance in quantifying forecast uncertainty. Although the HUP-BMA method has a higher CR value, its IW value is larger, and the PUCI value is smaller for the long forecast horizon, indicating that the forecast interval is too conservative to estimate the uncertainty range reasonably.

In order to visually analyze the ability of the CHUP-BMA method to quantify forecast uncertainty, the forecast intervals with a 90% confidence level of the HUP-BMA and CHUP-BMA methods for 168h forecast horizon in the 2020 flood season are compared. It can be seen from Fig.11 that the forecast intervals of the two ensemble forecasts can cover most of the observed flows and always cover the annual maximum flood peak, indicating that the forecast intervals are reliable. Meanwhile, the forecast intervals of the CHUP-BMA method are remarkably narrower than those of the HUP-BMA method, indicating that the forecast uncertainty of the former is relatively low, which can provide more reasonable risk information for TGR flood control decisions.

## (2) Evaluation of overall probabilistic forecast

Fig.12 shows the PIT histograms of the HUP-BMA and CHUP-BMA methods for 24, 96, and 168h forecast horizons. It can be significantly observed that the PIT plots of the HUP-BMA method show a  $\cap$ -shaped distribution, which indicates that the forecast distribution is over-dispersed and overestimates the forecast uncertainty, explaining the phenomenon of wide intervals. Meanwhile, the PIT plot of CHUP-BMA is more uniformly distributed than that of the HUP-BMA method, which can obtain a better calibration performance.





512

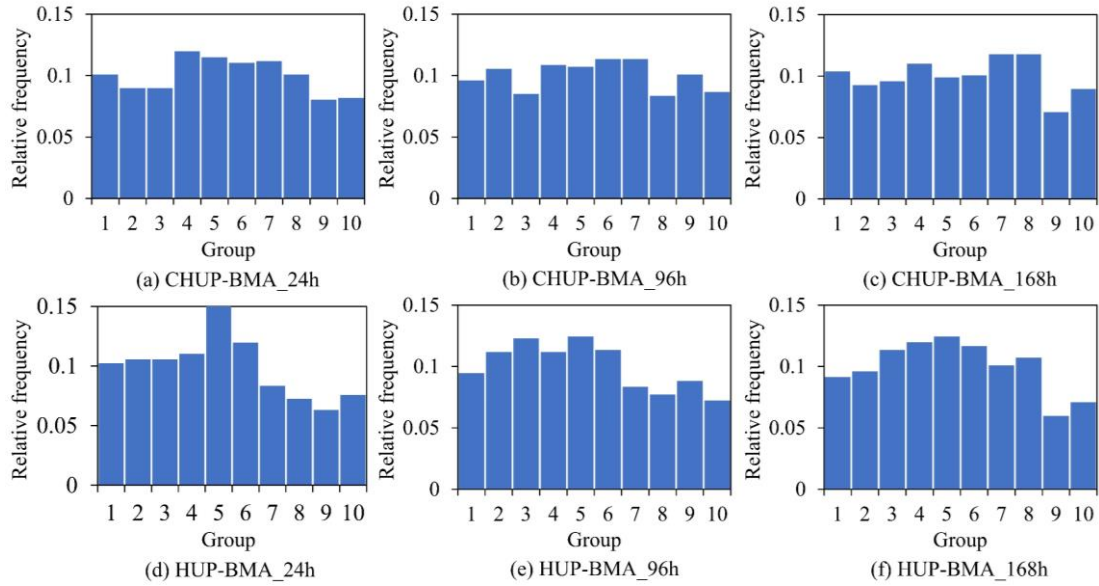
513 **Fig. 11** Forecast intervals with the 90% confidence level for the HUP-BMA and CHUP-BMA methods from 2020/7/1 8:00 to 9/24 8:00

514

515 Meanwhile, Fig.13(a), (b), and (c) show the evaluation metrics of  $\alpha$ \_index, IGS, and CRPS metrics for the two  
 516 ensemble probabilistic forecasts, respectively. It can be seen from Fig. 13(a) that the  $\alpha$ \_index metrics of the CHUP-BMA  
 517 method-based probabilistic forecasts are significantly higher than those of the HUP-BMA method in the 6-168h forecast  
 518 horizons. Among them, the maximum, minimum, and mean of the  $\alpha$ \_index metric for CHUP-BMA method-based  
 519 probabilistic forecasts are 0.98, 0.93, and 0.97, respectively, and 0.95, 0.88, and 0.93 for the HUP-BMA method,  
 520 respectively. The  $\alpha$ \_index metric of the CHUP-BMA method-based probabilistic forecast is closer to the perfect value of 1,  
 521 indicating that its probability forecast is the more reliable.

522

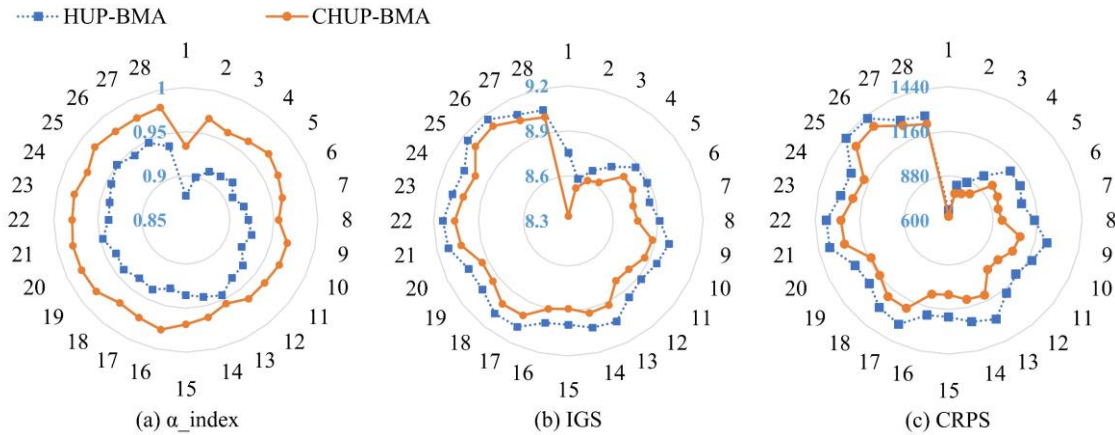
It can be seen from Fig.13(b) that the IGS values of the two methods gradually increase with the increase of the forecast  
 523 horizon, indicating that the forecast uncertainty gradually increases. The maximum, minimum, and mean of the IGS metric  
 524 for the CHUP-BMA method are 9.10, 8.33, and 8.87, respectively, and 9.16, 8.59, and 8.98 for the HUP-BMA method,  
 525 respectively. It can be seen that the IGS metrics of the CHUP-BMA method are consistently lower than those of the HUP-  
 526 BMA method, which indicates that the CHUP-BMA method has better ensemble forecast performance relative to the HUP-  
 527 BMA method by assigning a higher probability density around the actual values.



529

530 **Fig. 12** The probability integral transform (PIT) histograms of the HUP-BMA and CHUP-BMA methods for the ensemble forecasts of the  
 531 24, 96, and 168h forecast horizons.

532



533

534 **Fig. 13** Evaluation metrics of  $\alpha$ \_index, IGS, and CRPS metrics of two ensemble forecasts. The  $\alpha$ \_index metric can assess the reliability of  
 535 ensemble forecasts, while the IGS and CRPS metrics can reflect the reliability and sharpness of the ensemble forecast. The closer the  
 536  $\alpha$ \_index metric is to 1, and the smaller the IGS and CRPS metrics are, the better the performance of the ensemble forecast.

537

538 As shown in Fig. 13(c), the CRPS values of the two methods are lower than the MAE values of the selected member  
 539 (Fig. 8(b)), indicating that the probabilistic forecasts are effective and can fit the probabilistic distribution of the target values  
 540 well. Meanwhile, during the 6-168h forecast horizons, the maximum, minimum, and mean of the CRPS metric for the  
 541 CHUP-BMA method are 1356, 625, and 1074 m<sup>3</sup>/s, respectively, and 1425, 662, and 1188 m<sup>3</sup>/s for the HUP-BMA method,

542 respectively. It can be seen that the CRPS values of the CHUP-BMA method are lower than those of the HUP-BMA method,  
 543 with a maximum and average reduction of 17.86% and 9.71%, respectively. It can be seen that the CHUP-BMA method can  
 544 better fit the posterior distribution of the actual values and effectively improve the probabilistic forecast performance of the  
 545 HUP-BMA method.

546 From the Table 5, it can be seen that the T-statistics at the 0.05 significance level for all three metrics are higher than  
 547 the threshold value, indicating that there is a significant difference between the scores of the CHUP-BMA and HUP-BMA  
 548 methods, i.e., the CHUP-BMA method is significantly better than the HUP-BMA method for ensemble forecasting metrics  
 549 and performance.

550

551 Table 5 T-test results of ensemble forecast metrics at 0.05 significance level

Metric	$\alpha$ _index		IGS		CRPS	
	HUP-BMA	CHUP-BMA	HUP-BMA	CHUP-BMA	HUP-BMA	CHUP-BMA
Mean	0.93	0.97	8.98	8.87	1188	1074
Variance	0.0003	0.0001	0.02	0.03	32247	33716
Degree of freedom	46.00		52.00		54.00	
T-statistic	-10.76		2.36		2.34	
T-threshold	1.68		1.67		1.67	
Difference significance analysis	Significant		Significant		Significant	

552

553 In summary, the CHUP-BMA method considers the influence of the initial state on the ensemble forecast, bypasses the  
 554 normal quantile transformation of the HUP-BMA method, derives the posterior distribution of the target flow without  
 555 restrictions, and improves the probabilistic forecast performance of the HUP-BMA method. Therefore, the ensemble  
 556 forecasting by CHUP-BMA method can provide more reasonable and reliable risk information for the TGR.

## 557 5 Conclusion and prospects

558 In this study, we proposed a novel CHUP-BMA method, which not only can consider the influence of the initial state on  
 559 the ensemble forecast, but also can avoid the assumption of normal distribution in the HUP-BMA method and derive the  
 560 posterior distribution function more accurately. An ensemble forecast scheme that consists of two forecasted precipitation,  
 561 two hydrological models, and two objective functions of parameter calibration was established. The ensemble forecasting  
 562 performance of the HUP-BMA and CHUP-BMA methods was discussed from the perspective of deterministic and  
 563 probabilistic forecasts. The flood ensemble forecasting experiment with 6-168h forecast horizons was conducted in the  
 564 Xiangjiaba-TGR dam-site interval basin. The main conclusions were summarized as follows.

565 (1) The two ensemble forecasting methods can improve the members' forecast accuracy. The proposed CHUP-BMA  
566 method performs better than the HUP-BMA method, and the MAE metric is reduced by a maximum of 10.69% within 6-  
567 168h forecast horizons.

568 (2) The coverage rate of the forecast interval of the CHUP-BMA method is close to or exceeds the specified 90%  
569 confidence level, and the forecast interval is significantly narrower than that of the HUP-BMA method, with a maximum  
570 reduction of 28.42% during 6-168h forecast horizons, which can effectively reduce the forecast uncertainty.

571 (3) The probabilistic forecast of the CHUP-BMA method has better reliability and sharpness, and its CRPS values are  
572 reduced by a maximum of 17.86% relative to the HUP-BMA method, which indicates that the CHUP-BMA method can  
573 better fit the posterior distribution of the actual values.

574 (4) The CHUP-BMA method can derive the posterior distribution of the target flow without restriction under the  
575 condition of considering the initial constraint, which makes the BMA method more towards perfection. Therefore, it is more  
576 suitable for the flood forecasting in the 6-168h forecast horizons and provides reliable risk information for reservoir  
577 scheduling decision-making.

578 The present study focuses on flood ensemble forecasting for the TGR's 6-168h forecast horizons. Future studies can  
579 explore the ensemble forecasting performance of the proposed CHUP-BMA method for longer forecast horizons and further  
580 validate the effectiveness of the proposed method in global basins. Meanwhile, the vine copula, which facilitates multivariate  
581 joint distribution modelling, can be considered for constructing the CHUP-BMA method and exploring its advantages and  
582 effectiveness in ensemble flood forecasting. And the effective way or method of guiding reservoir scheduling based on  
583 ensemble forecasts can be further explored so that ensemble forecasts can be widely used in decision-making.

## 584 **Appendix A: The model parameters for ensemble membership**

585 We set the number of neural network layers and neurons to be the same for the encoding and decoding processes, with  
586 trial-and-error preferences for the number of hidden layers, neurons, and dropout. Meanwhile, the batch size, epoch, and  
587 learning rate are set to 100, 500, and 0.001, respectively. The different model parameters are shown in Table A1.

588

589

**Table A1** The model parameters for ensemble membership

Ensemble member type	Neuron	Hidden layers	Dropout
ECMWF&DA-LSTM-RED&MSE	64	1	0.001
ECMWF&LSTM-RED&MSE	64	1	0.001
ECMWF&DA-LSTM-RED&MAE	32	1	0.01
ECMWF&LSTM-RED&MAE	64	1	0.1
HBYRWRC &DA-LSTM-RED&MSE	32	1	0.1

HBYRWRC &LSTM-RED&MSE	32	1	0.001
HBYRWRC &DA-LSTM-RED&MAE	64	1	0.001
HBYRWRC &LSTM-RED&MAE	48	1	0.01

---

590

591 **Code availability**

592 The code used to support the findings of this study are available from the corresponding author upon request.

593 **Data availability**

594 The data generated and/or analyzed during the current study are not publicly available for legal/ethical reasons but are  
595 available from the corresponding author on reasonable request.

596 **Author contributions**

597 Zhen Cui and Shenglian Guo conceived and designed the experiments; Zhen Cui performed the experiments and wrote the  
598 manuscript draft; Zhen Cui, Shenglian Guo, Chong-Yu Xu, Hua Chen, Dedi Liu, and Yanlai Zhou reviewed and edited the  
599 manuscript.

600 **Competing interests**

601 The authors declare that they have no conflict of interest.

602 **Acknowledgments**

603 This study was financially supported by the National Key Research and Development Program of China (2022YFC3202801,  
604 2021YFC3200305), and China Three Gorges Cooperation (0799254).

605 **References**

606 Baran, S., Hemri, S. and El Ayari, M. Statistical post-processing of water level forecasts using Bayesian model averaging  
607 with doubly-truncated normal components. *Water Resour. Res.* 55, 3997–4013. <https://doi.org/10.1029/2018WR024028>,  
608 2019.

609 Biondi, D., and Todini, E. Comparing hydrological postprocessors including ensemble predictions into full predictive  
610 probability distribution of streamflow. *Water Resour. Res.*, 54(12), 9860-9882, <https://doi.org/10.1029/2017WR022432>,  
611 2018.

612 Chen, L., and Guo, S. Copulas and its application in hydrology and water resources. Springer Water, Springer Singapore,  
613 <https://doi.org/10.1007/978-981-13-0574-0>, 2019.

614 Cho, K., and Kim, Y. Improving streamflow prediction in the WRF-Hydro model with LSTM networks. *J. Hydrol.*, 605,  
615 127297. <https://doi.org/10.1016/j.jhydrol.2021.127297>, 2022.

616 Cloke, H. L., and Pappenberger, F. Ensemble flood forecasting: A review. *J. Hydrol.*, 375(3-4), 613-626.  
617 <https://doi.org/10.1016/j.jhydrol.2009.06.005>, 2009.

618 Cui, Z., Guo, S., Zhou, Y., Wang, J. Exploration of dual-attention mechanism-based deep learning for multi-step-ahead flood  
619 probabilistic forecasting. *J. Hydrol.*, 622, 129688. <https://doi.org/10.1016/j.jhydrol.2023.129688>, 2023.

620 Cui, Z., Zhou, Y., Guo, S., Wang, J., and Xu, C. Y. Effective improvement of multi-step-ahead flood forecasting accuracy  
621 through encoder-decoder with an exogenous input structure. *J. Hydrol.*, 609, 127764.  
622 <https://doi.org/10.1016/j.jhydrol.2022.127764>, 2022.

623 Darbandsari, P., and Coulibaly, P. Introducing entropy-based Bayesian model averaging for streamflow forecast. *J. Hydrol.*,  
624 591, 125577. <https://doi.org/10.1016/j.jhydrol.2020.125577>, 2020.

625 Darbandsari, P., and Coulibaly, P. HUP-BMA: An Integration of Hydrologic Uncertainty Processor and Bayesian Model  
626 Averaging for Streamflow Forecasting. *Water Resour. Res.*, 57(10), e2020WR029433.  
627 <https://doi.org/10.1029/2020WR029433>, 2021.

628 Ding, Y., Zhu, Y., Feng, J., Zhang, P., and Cheng, Z. Interpretable spatial-temporal attention LSTM model for flood  
629 forecasting. *Neurocomputing*, 403, 348-359. <https://doi.org/10.1016/j.neucom.2020.04.110>, 2020.

630 Duan, Q., Ajami, N. K., Gao, X., and Sorooshian, S. Multi-model ensemble hydrologic prediction using Bayesian model  
631 averaging. *Adv. Water Resour.*, 30(5), 1371-1386. <https://doi.org/10.1016/j.advwatres.2006.11.014>, 2007.

632 Fedora, M. A., and Beschta, R. L. Storm runoff simulation using an antecedent precipitation index (API) model. *J. Hydrol.*,  
633 112(1-2), 121-133. [https://doi.org/10.1016/0022-1694\(89\)90184-4](https://doi.org/10.1016/0022-1694(89)90184-4), 1989.

634 Ferretti, R., Lombardi, A., Tomassetti, B., Sangelantoni, L., Colaiuda, V., Mazzarella, V., Maiello, I., Verdecchia, M., and  
635 Redaelli, G.: A meteorological–hydrological regional ensemble forecast for an early-warning system over small Apennine  
636 catchments in Central Italy, *Hydrol. Earth Syst. Sci.*, 24, 3135–3156, <https://doi.org/10.5194/hess-24-3135-2020>, 2020.

637 Gelfan, A., Moreydo, V., Motovilov, Y., and Solomatine, D. P. Long-term ensemble forecast of snowmelt inflow into the  
638 Cheboksary Reservoir under two different weather scenarios. *Hydrol. Earth Syst. Sci.*, 22(4), 2073-2089.  
639 <https://doi.org/10.5194/hess-22-2073-2018>, 2018.

640 Gneiting, T., Raftery, A. E., Westveld, A. H., and Goldman, T. Calibrated probabilistic forecasting using ensemble model  
641 output statistics and minimum CRPS estimation. *Mon. Weather Rev.*, 133(5), 1098-1118.  
642 <https://doi.org/10.1175/MWR2904.1>, 2005.

643 Guo, Y., Yu, X., Xu, Y. P., Chen, H., Gu, H., and Xie, J. AI-based techniques for multi-step streamflow forecasts:  
644 application for multi-objective reservoir operation optimization and performance assessment. *Hydrol. Earth Syst. Sci.*,  
645 25(11), 5951-5979. <https://doi.org/10.5194/hess-25-5951-2021>, 2021.

646 Han, S., and Coulibaly, P. Bayesian flood forecasting methods: A review. *J. Hydrol.*, 551, 340-351.  
647 <https://doi.org/10.1016/j.jhydrol.2017.06.004>, 2017.

648 Hauswirth, S. M., Bierkens, M. F., Beijck, V., and Wanders, N. The suitability of a seasonal ensemble hybrid framework  
649 including data-driven approaches for hydrological forecasting. *Hydrol. Earth Syst. Sci.*, 27(2), 501-517.  
650 <https://doi.org/10.5194/hess-27-501-2023>, 2023.

651 Hemri, S., Fundel, M. and Zappa, M. Simultaneous calibration of ensemble river flow predictions over an entire range of  
652 lead times. *Water Resour. Res.* 49, 6744–6755. <https://doi.org/10.1002/wrcr.20542>, 2013.

653 Hochreiter, S., Schmidhuber, J. Long short-term memory. *Neural Computation*, 9(8), 1735-1780.  
654 <https://doi.org/10.1162/neco.1997.9.8.1735>, 1997.

655 Huang, H., Liang, Z., Li, B., Wang, D., Hu, Y., and Li, Y. Combination of multiple data-driven models for long-term  
656 monthly runoff predictions based on Bayesian model averaging. *Water Resour. Manag.*, 33, 3321-3338.  
657 <https://doi.org/10.1007/s11269-019-02305-9>, 2019.

658 Kao, I. F., Zhou, Y., Chang, L. C., and Chang, F. J. Exploring a Long Short-Term Memory based Encoder-Decoder  
659 framework for multi-step-ahead flood forecasting. *J. Hydrol.*, 583, 124631. <https://doi.org/10.1016/j.jhydrol.2020.124631>,  
660 2020.

661 Kingma D P, Ba J. Adam: A method for stochastic optimization. arXiv preprint arXiv:1412.6980, [https://doi.org/10.48550/ar](https://doi.org/10.48550/arXiv.1412.6980)  
662 [Xiv.1412.6980](https://doi.org/10.48550/arXiv.1412.6980), 2014.

663 Kratzert, F., Klotz, D., Brenner, C., Schulz, K., Herrnegger, M. Rainfall–runoff modelling using long short-term memory  
664 (LSTM) networks. *Hydrology and Earth System Sciences*, 22(11), 6005-6022. <https://doi.org/10.5194/hess-22-6005-2018>,  
665 2018.

666 Krzysztofowicz, R. Bayesian theory of probabilistic forecasting via deterministic hydrologic model. *Water Resour. Res.*,  
667 35(9), 2739-2750. <https://doi.org/10.1029/1999WR900099>, 1999.

668 Krzysztofowicz, R., and Kelly, K. S. Hydrologic uncertainty processor for probabilistic river stage forecasting. *Water Resour.*  
669 *Res.*, 36(11), 3265-3277. <https://doi.org/10.1029/2000WR900108>, 2000.

670 Kussul, N., Shelestov, A., and Skakun, S. Grid system for flood extent extraction from satellite images. *Earth Sci. Inform.*, 1,  
671 105-117. <https://doi.org/10.1007/s12145-008-0014-3>, 2008.

672 Li, D., Marshall, L., Liang, Z., Sharma, A., Zhou, Y. Bayesian LSTM with stochastic variational inference for estimating  
673 model uncertainty in process-based hydrological models. *Water Resources Research*, 57(9), e2021WR029772.  
674 <https://doi.org/10.1029/2021WR029772>, 2021.

675 Li, L., Xu, C. Y., Xia, J., Engeland, K., and Reggiani, P. Uncertainty estimates by Bayesian method with likelihood of AR (1)  
676 plus Normal model and AR (1) plus Multi-Normal model in different time-scales hydrological models. *J. Hydrol.*, 406(1-2),  
677 54-65. <https://doi.org/10.1016/j.jhydrol.2011.05.052>, 2011.

678 Li, W., Duan, Q., Miao, C., Ye, A., Gong, W., and Di, Z. A review on statistical postprocessing methods for  
679 hydrometeorological ensemble forecasting. *Wiley Interdiscip. Rev.-Water*, 4(6), e1246. <https://doi.org/10.1002/wat2.1246>,  
680 2017.

681 Liu, J., Yuan, X., Zeng, J., Jiao, Y., Li, Y., Zhong, L., and Yao, L. Ensemble streamflow forecasting over a cascade reservoir  
682 catchment with integrated hydrometeorological modeling and machine learning. *Hydrol. Earth Syst. Sci.*, 26(2), 265-278.  
683 <https://doi.org/10.5194/hess-26-265-2022>, 2022.

684 Liu, Z., Guo, S., Xiong, L., and Xu, C. Y. Hydrological uncertainty processor based on a copula function. *Hydrol. Sci. J.-J.*  
685 *Sci. Hydrol.*, 63(1), 74-86. <https://doi.org/10.1080/02626667.2017.1410278>, 2018.

686 Liu, Z., Guo, S., Zhang, H., Liu, D., and Yang, G. Comparative study of three updating procedures for real-time flood  
687 forecasting. *Water Resour. Manag.*, 30, 2111-2126. <https://doi.org/10.1007/s11269-016-1275-0>, 2016.

688 Madadgar, S., and Moradkhani, H. Improved Bayesian multi-modelling: Integration of copulas and Bayesian model  
689 averaging. *Water Resour. Res.*, 50(12), 9586-9603. <https://doi.org/10.1002/2014WR015965>, 2014.

690 Matthews, G., Barnard, C., Cloke, H., Dance, S. L., Jurlina, T., Mazzetti, C., and Prudhomme, C. Evaluating the impact of  
691 post-processing medium-range ensemble streamflow forecasts from the European Flood Awareness System. *Hydrol. Earth*  
692 *Syst. Sci.*, 26(11), 2939-2968. <https://doi.org/10.5194/hess-26-2939-2022>, 2022.

693 Nash, J. E., and Sutcliffe, J. V. River flow forecasting through conceptual models: part I—A discussion of principles. *J.*  
694 *Hydrol.*, 10(3), 282-290. [https://doi.org/10.1016/0022-1694\(70\)90255-6](https://doi.org/10.1016/0022-1694(70)90255-6), 1970.

695 Parrish, M. A., Moradkhani, H., and DeChant, C. M. Toward reduction of model uncertainty: Integration of Bayesian model  
696 averaging and data assimilation. *Water Resour. Res.*, 48(3). <https://doi.org/10.1029/2011WR011116>, 2012.

697 Qin, Y., Song, D., Chen, H., Cheng, W., Jiang, G., and Cottrell, G. A dual-stage attention-based recurrent neural network for  
698 time series prediction. *arXiv preprint arXiv:1704.02971*. <https://doi.org/10.48550/arXiv.1704.02971>, 2017.

699 Raftery, A. E., Gneiting, T., Balabdaoui, F., and Polakowski, M. Using Bayesian model averaging to calibrate forecast  
700 ensembles. *Mon. Weather Rev.*, 133(5), 1155-1174. <https://doi.org/10.1175/MWR2906.1>, 2005.

701 Renard, B., Kavetski, D., Kuczera, G., Thyer, M., and Franks, S. W. Understanding predictive uncertainty in hydrologic  
702 modeling: The challenge of identifying input and structural errors. *Water Resour. Res.*, 46(5).  
703 <https://doi.org/10.1029/2009WR008328>, 2010.

704 Shu, Z., Zhang, J., Wang, L., Jin, J., Cui, N., Wang, G., ..., and Liu, C. Evaluation of the impact of multi-source uncertainties  
705 on meteorological and hydrological ensemble forecasting. *Engineering*. <https://doi.org/10.1016/j.eng.2022.06.007>, 2022.

706 Saleh, F., Ramaswamy, V., Georgas, N., Blumberg, A. F., and Pullen, J. A retrospective streamflow ensemble forecast for an  
707 extreme hydrologic event: a case study of Hurricane Irene and on the Hudson River basin. *Hydrol. Earth Syst. Sci.*, 20(7),  
708 2649-2667. <https://doi.org/10.5194/hess-20-2649-2016>, 2016.



709 Sklar, M. Fonctions de repartition an dimensions et leurs marges. *Publ. inst. statist. univ. Paris*, 8, 229-231. 1959.

710 Sloughter, J. M., Raftery, A. E., Gneiting, T. and Fraley, C. Probabilistic quantitative precipitation forecasting using  
711 Bayesian model averaging. *Mon. Weather Rev.* 135, 3209–3220. <https://doi.org/10.1175/MWR3441.1>, 2007

712 Sloughter, J. M., Gneiting, T., and Raftery, A. E. Probabilistic wind speed forecasting using ensembles and Bayesian model  
713 averaging. *J. Am. Stat. Assoc.*, 105(489), 25-35. <https://doi.org/10.1198/jasa.2009.ap08615>, 2010.

714 Todini, E. A model conditional processor to assess predictive uncertainty in flood forecasting. *Int. J. River Basin Ma.*, 6(2),  
715 123-137. <https://doi.org/10.1080/15715124.2008.9635342>, 2008.

716 Vegad, U., and Mishra, V. Ensemble streamflow prediction considering the influence of reservoirs in Narmada River Basin,  
717 India. *Hydrol. Earth Syst. Sci.*, 26(24), 6361-6378. <https://doi.org/10.5194/hess-26-6361-2022>, 2022.

718 Wei, L., Jiang, S., Dong, J., Ren, L., Liu, Y., Zhang, L., ..., and Duan, Z. Fusion of gauge-based, reanalysis, and satellite  
719 precipitation products using Bayesian model averaging approach: Determination of the influence of different input sources. *J.*  
720 *Hydrol.*, 618, 129234. <https://doi.org/10.1016/j.jhydrol.2023.129234>, 2023.

721 Xiang, Z., Yan, J., and Demir, I. A rainfall-runoff model with LSTM-based sequence-to-sequence learning. *Water Resour.*  
722 *Res.*, 56(1), e2019WR025326. <https://doi.org/10.1029/2019WR025326>, 2020.

723 Xiong, L., Wan, M. I. N., Wei, X., O'connor, K. M. Indices for assessing the prediction bounds of hydrological models and  
724 application by generalised likelihood uncertainty estimation. *Hydrological sciences journal*, 54(5), 852-871.  
725 <https://doi.org/10.1623/hysj.54.5.852>, 2009.

726 Xu, C., Zhong, P. A., Zhu, F., Yang, L., Wang, S., and Wang, Y. Real-time error correction for flood forecasting based on  
727 machine learning ensemble method and its uncertainty assessment. *Stoch. Environ. Res. Risk Assess.*, 1-21.  
728 <https://doi.org/10.1007/s00477-022-02336-6>, 2022.

729 Yang, T., Sun, F., Gentine, P., Liu, W., Wang, H., Yin, J., ..., and Liu, C. Evaluation and machine learning improvement of  
730 global hydrological model-based flood simulations. *Environmental Research Letters*, 14(11), 114027.  
731 <https://doi.org/10.1088/1748-9326/ab4d5e>, 2019.

732 Zhang, B., Wang, S., Qing, Y., Zhu, J., Wang, D., and Liu, J. A vine copula-based polynomial chaos framework for  
733 improving multi-model hydroclimatic projections at a multi-decadal convection-permitting scale. *Water Resour. Res.*, 58(6),  
734 e2022WR031954. <https://doi.org/10.1029/2022WR031954>, 2022.

735 Zhou, Y., Cui, Z., Lin, K., Sheng, S., Chen, H., Guo, S., and Xu, C. Y. Short-term flood probability density forecasting using  
736 a conceptual hydrological model with machine learning techniques. *J. Hydrol.*, 604, 127255.  
737 <https://doi.org/10.1016/j.jhydrol.2021.127255>, 2022.

738 Zhou, Y., Guo, S., and Chang, F. J. Explore an evolutionary recurrent ANFIS for modelling multi-step-ahead flood forecasts.  
739 *J. Hydrol.*, 570, 343-355. <https://doi.org/10.1016/j.jhydrol.2018.12.040>, 2019.

740 Zhong, Y., Guo, S., Ba, H., Xiong, F., Chang, F. J., and Lin, K. Evaluation of the BMA probabilistic inflow forecasts using  
741 TIGGE numeric precipitation predictions based on artificial neural network. *Hydrol. Res.*, 49(5), 1417-1433.  
742 <https://doi.org/10.2166/nh.2018.177>, 2018a.

743 Zhong, Y., Guo, S., Liu, Z., Wang, Y., and Yin, J. Quantifying differences between reservoir inflows and dam site floods  
744 using frequency and risk analysis methods. *Stoch. Environ. Res. Risk Assess.*, 32, 419-433. [https://doi.org/10.1007/s00477-](https://doi.org/10.1007/s00477-017-1401-4)  
745 017-1401-4, 2018b.

746 Zhong, Y., Guo, S., Xiong, F., Liu, D., Ba, H., and Wu, X. Probabilistic forecasting based on ensemble forecasts and EMOS  
747 method for TGR inflow. *Front. Earth Sci.*, 14, 188-200. <https://doi.org/10.1007/s11707-019-0773-9>, 2020.

748